Synthesis and Characterization of WSe_2 Nanosheets and WS_2 Quantum Dots for Electronics and Optoelectronics Device Applications

By

ANKITA BANERJEE

Registration No. **150147** of 2019-2020

Examination Roll No. **M6VLS22019**

Under the Guidance of

Dr. Divya Somvanshi

Thesis Submitted in partial fulfilment of the requirement for the award of the Degree of Master of Technology in VLSI Design and Microelectronics Technology

Department of Electronics & Telecommunication Engineering

Kolkata-700032

West Bengal, India

JUNE 2022

FACULTY OF ENGINEERING AND TECHNOLOGY

JADAVPUR UNIVERSITY

CERTIFICATE OF RECOMMENDATION

I hereby recommend that this Thesis prepared by **Ankita Banerjee** entitled **"Synthesis and Characterization of WSe_2 Nanosheets and WS_2 Quantum Dots for Electronics and Optoelectronic Device Applications"** under my supervision be accepted for partial fulfilment of the requirements for the award of the Degree of Master of Technology in VLSI Design and Microelectronics Technology under Electronics and Tele-Communication Engineering Department.

.....

Dr. Divya Somvanshi
Thesis Supervisor
Department of Electronics and Tele-Communication Engineering
Jadavpur University, Kolkata – 700032

....

Dr. Ananda Shankar Chowdhury
Professor and Head of the Department
Department of Electronics and
Tele-Communication Engineering,
Jadavpur University, Kolkata – 700032

Prof. Chandan Mazumdar
Dean
Faculty Council of Engineering and Technology
Jadavpur University, Kolkata – 700032

FACULTY OF ENGINEERING & TECHNOLOGY

JADAVPUR UNIVERSITY

DEPARTMENT OF ELECTRONICS & TELECOMMUNICATION ENGINEERING

CERTIFICATE OF APPROVAL*

The foregoing Thesis is hereby approved as a credible study of an Engineering subject and presented in a manner satisfactory to warrant acceptance as pre-requisite to the degree for which it has been submitted. It is understood that by this approval the undersigned do not necessarily endorse or approve any statement made, opinion expressed or conclusion drawn therein but approve the thesis only for which it is submitted.

Committee on

Final examination for

Evaluation of the thesis of:

ANKITA BANERJEE

Exam Roll No: **M6VLS22019**

_____

External Examiner

Dr. Divya Somvanshi

Department of Electronics &
Telecommunication Engineering
Jadavpur University
Kolkata-700032

*Only in case the thesis is approved.

FACULTY OF ENGINEERING & TECHNOLOGY

JADAVPUR UNIVERSITY

DECLARATION OF ORAGINALITY AND COMPLIANCE OF ACADEMIC ETHICS

It is hereby declared that this Thesis entitled **"Synthesis and Characterization of WSe_2 Nanosheets and WS_2 Quantum Dots for Electronics and Optoelectronic Device Applications"** contains original research work by the undersigned candidate, as a part of his degree of **Master of Technology in VLSI Design and Microelectronics Technology**.

All information has been obtained and presented in accordance with academic rules and ethical conduct.

It is also asserted that, as required by these rules and conduct, the undersigned has fully cited and referenced all materials and results that are not original to this work.

Name: ANKITA BANERJEE

Examination Roll No.: M6VLS22019

Thesis Title: "Synthesis and Characterization of WSe_2 Nanosheets and WS_2 Quantum Dots for Electronics and Optoelectronic Device Applications".

Signature of the Candidate: _____

Date:

ACKNOWLEDGEMENT

The success and final outcome of my thesis required a lot of guidance and assistance from many people and I am extremely fortunate to have got this all along the completion of my thesis work. Whatever I have done is only due to such guidance and assistance and I would not forget to thank them.

First and foremost, I owe my profound gratitude to my project supervisor, **Dr. Divya Somvanshi** who guided me till the completion of my project work by providing her precious advices and constant support. I would like to express my special appreciation and thanks to her for giving her full effort in guiding me to maintain the progress. She has been a tremendous mentor for me because without his invaluable suggestions and her continued motivation, my project work would not have taken a worthwhile shape.

I am thankful to and fortunate enough to get such a nice support, devotion and constant encouragement from my senior, Mrs. Sayantika Chowdhury throughout my thesis work. She has supported me in guiding, inspired me to strive towards my goal.

I would not forget to remember all the members specially Mr. Ashoke Mondal, and Mr. Bikash Bhowmik of IC Centre, Department of Electronics and Telecommunication Engineering, Jadavpur University for their unlisted inspirations and insightful suggestions till my project work completed.

I would like to thank H.O.D Department of Electronics & Telecommunication Engineering, Jadavpur University by providing me all the facilities for carrying out the entire project work. I would like to express my sincere appreciation to all the teaching and non-teaching staff of the department for providing necessary support and aids.

Last but not the least, a special heartfelt thanks to my beloved family. Words cannot express how grateful I am to my parents for all of the sacrifices that they have made on my behalf. Their prayer for me was what sustained me thus far.

_____

ANKITA BANERJEE

Date:

Place: Kolkata

LIST OF FIGURES

Fig. No.	Figure Name	Page No.
	Chapter 1	
Fig: 1.1	Periodic table of elements presenting the possible combinations of elements forming layered TMDCs MX_2	3
Fig: 1.2	Two single crystal of WX_2 (X = S, Se)(TMDC materials)	4
Fig:1.3	Layered structure of WX_2 monolayer and bilayer (in 2D and 3D) structure	5
Fig.1.4	Band Structure of WSe_2 (a) Bulk (b) Monolayer (c) Bi-layer simulated by using Quantum ATK	7
Fig. 1.5	Band Structure of WS_2 (a) Bulk (b) Monolayer (c) Bi-layer simulated by using Quantum ATK	7
Fig.1.6	Schematic diagram showing energy band structures in atom, bulk material, and quantum nanostructure.	9
Fig.1.7	Schematic diagram for the formation of discrete energy levels.	9
Fig. 1.8	Schematic diagram of Transmission Electron Microscopy (TEM)	17
Fig. 1.9	Structure of Scanning Electron Microscopy	18
Fig. 1.10	Working principle of AFM	19
Fig. 1.11	Three basic working modes of AFM	20
Fig. 1.12	Bragg's Law	21

Fig. 1.13	**Block Diagram of UV-Vis Spectroscopy**	**23**
Fig. 1.14	**Structural diagram of photoluminescence spectroscopy**	**24**
Fig. 1.15	**Block Diagram of Photoluminescence Spectroscopy (PL)**	**24**
Fig. 1.16	**Molecular vibrations and Raman scattering**	**25**
Fig. 1.17	**Raman Scattering diagram of Raman Spectroscopy**	**26**

Chapter 3

Fig. 3.1	**Different steps of Colloidal synthesis process for WSe_2 Nanosheets**	**33**
Fig. 3.2	**(a) Photo image of as-prepared WSe_2-NSs solution before annealing (b) WSe_2 NSs powder after annealing at 200°C for 2 hrs (c) WSe_2 NSs solution dispersed in DI water for further use. (d) WSe_2 NSs under UV light to show the luminescence.**	**34**
Fig. 3.3	**Different steps of colloidal synthesis process for WS_2 Quantum dots**	**35**
Fig. 3.4	**(a) Photo image of as-prepared WS_2-QDs solution (b) WS_2 QDs solution after filtration by dialysis bag for 2-3 days. (c) WS_2 QDs under UV light to show the luminescence.**	**35**

Chapter 4

Fig. 4.1	**SEM images of WSe_2 nanosheet (powder sample)**	**39**
Fig. 4.2	**(a) TEM images of WSe_2 Nanosheets (b) HRTEM images of WSe_2 Nanosheet edges**	**40**
Fig. 4.3	**The XRD of WSe_2 Nanosheets (powder sample)**	**41**
Fig. 4.4	**(a) PL-Spectrum of WSe_2 Nanosheets for different excitation. (b) Excitation and emission PL spectra of WSe_2 Nanosheets**	**43**
Fig. 4.5	**(a) The Absorption spectra of WSe_2 Nanosheets**	**44**
Fig. 4.6	**The Raman spectra of WSe_2 Nanosheets prepared using hydrothermal method**	**45**
Fig. 4.7	**(a) AFM image of WS_2 QDs based thin film coated on Si substrate (b) Height profile of WS_2 QDs**	**46**
Fig. 4.8	**The XRD pattern of WS_2 Quantum Dots based thin film coated on Si substrate**	**47**
Fig. 4.9	**a) Absorption spectra (b) Energy-Band gap calculations of WS_2 QDs**	**49**
Fig. 4.10	**(a) PL-Spectrum of WS_2 QDs for different excitation. (b) Excitation and emission PL spectra of WS_2 QDs**	**51**
Fig. 4.11	**The Raman spectra of WS_2 Quantum Dots**	**52**

Chapter 5

Fig 5.1	**Schematic Device Structure of Al/Ti/n-Si/p-WSe_2/n-WS_2/Ag and Al/Ti/n-Si/n-WS_2/p-WSe_2/Ag**	**55**
Fig 5.2	**Schematic Device Structure of Al/Ti/p-Si/WS_2/Ag**	**55**

LIST OF TABLES

Table No.	Table Name	Page No.
	Chapter 1	
Table 1.1	Classification of quantum confined structures	10

TABLE OF CONTENTS

INDEX

CONTENT **PAGE NO.**

Certificate of Recommendation

Certificate of Approval

Declaration of originality and Compliance of Academic Ethics

Acknowledgement

List of Figures

List of Tables

- Abstract 1

CHAPTER 1: INTRODUCTION

1.1 Two-dimensional (2D) Materials 2

1.2 Transition Metal Dichalcogenides (TMDC) Materials 2-3

1.3 Tungsten disulfide and Tungsten diselenide Properties 4

1.3.1 Crystal Structure 4-5

1.3.2 Band Structure 5-8

1.4 Quantum Confinement 8-10

1.4.1 Particle in Quantum Confined Structure 11-13

1.5 Synthesis Methods

1.5.1 Micromechanical Exfoliation 14

1.5.2 Liquid Exfoliations 14

1.5.3 Chemical Vapour Deposition 15

1.5.4 Hydrothermal Synthesis 15

1.6 Characterization Method 16

1.6.1 Transmission Electron Microscopy (TEM) 16-17

1.6.2 Scanning Electron Microscopy (SEM) 17-18

1.6.3 Atomic Force Microscopy (AFM) 19-20

1.6.4 X-ray Diffraction (XRD) 21-22

1.6.5 UV-Visible Spectroscopy 22-23
1.6.6 Photoluminescence Spectroscopy (PL) 23-24
1.6.7 Raman Spectroscopy 24-26
1.7 Motivation 26

CHAPTER 2: LITERATURE REVIEW

2.1 Introduction 27
2.2 Literature Review 27-30

CHAPTER 3: SYNTHESIS OF WSe_2 NANOSHEETS AND WS_2 QUANTUM DOTS ON Si SUBSTRATES

3.1 Introduction 31
3.2 Preparation of WSe_2 Nanosheets and WS_2 Quantum Dots by Hydrothermal Method 31
3.3 Experimental Section
3.3.1 Chemical Required 32
3.3.2 Synthesis of WSe_2 Nanosheets 32-34
3.3.3 Synthesis of WS_2 Quantum Dots 34-35
3.4 Sample preparation for Characterization
3.4.1 Wafer cleaning 36
3.4.2 Glass Slide cleaning 36-37
3.4.3 Characterization Technique 37

CHAPTER 4: STRUCTURAL, MORPHOLOGICAL AND OPTICAL CHARACTERIZATION OF WSe_2 NANOSHEETS AND WS_2 QUANTUM DOTS ON Si SUBSTRATES

4.1 Structural and Morphological studies of WSe_2 Nanosheets 38
4.1.1 SEM Characterization 38-39
4.1.2 TEM Characterization 39-40
4.1.3 XRD pattern 41

4.2 Optical Property studies of WSe_2 Nanosheets 42
4.2.1 PL spectra 42-43
4.2.2 UV-Visible spectra 43-44
4.2.3 Raman spectra 44-45
4.3 Structural Characterization of WS_2 Quantum Dots 45
4.3.1 AFM Characterization 45-46
4.3.2 XRD pattern 46-47
4.4 Optical Property studies of WS_2 Quantum Dots 47
4.4.1 PL spectra 47-49
4.4.2 UV-Visible spectra 50-51
4.4.3 Raman spectra 51-52

CHAPTER 5: CONCLUSION AND FUTURE SCOPE

5.1 Introduction 53-54
5.2 Future Scope 54-55
5.3 References 55-59

ABSTRACT

Two-dimensional (2D) transition metal dichalcogenide (2D-TMDC) semiconductors have attracted significant attention because of their unique physical properties which are very important for fundamental and applied research. Due to the variety of properties owing to their layer dependent optical bandgap variation efficient charge transfer and strong light-matter interactions; TMDC materials provides a stand that allows to create of larger range of device for various applications. In recent advances, in the development of nanostructures of 2D materials, the zero-dimensional (0D) quantum dots (QDs) offered new possibilities for the broad range photodetectors, bio imaging, batteries, electrochemical water splitting and optoelectronic applications because of their intriguing optical, electrical, catalytic and electrochemical properties. QDs derived from TMDC, specifically molybdenum disulfide (MoS_2), are gaining popularity due to their advantageous properties in optoelectronics, imaging, and sensors. Despite this, little research has been conducted to synthesize and investigate photoluminescent 0D Tungsten disulfide (WS_2) QDs, particularly using a bottom-up approach without the use of typical toxic organic solvents. TMDCs nanosheets (NSs) are ultrathin two-dimensional materials that are fundamentally and technologically intriguing. They are more chemically versatile than graphene sheets. Mono- or few-layered TMDCs are direct/indirect-bandgap semiconductors with varying bandgap energy and carrier type (n- or p-type) depending on composition, structure, and dimensionality. In this thesis, we will discuss about the recent research advancement with emphasising on synthesis, optical and structural characterization of WSe_2 NSs on n-Si substrate and WS_2 QDs on p-Si substrate. Here I present a simple bottom-up strategy for producing high-quality water-soluble tungsten disulfide (WS_2) QDs via hydrothermal reaction with sodium tungstate dihydrate and L-cysteine as W and S sources. Along with, we have also synthesised tungsten diselenide (WSe_2) nanosheets by using hydrothermal technique using Sodium tungstate dihydrate ($Na_2WO_4 \cdot 2H_2O$)) as a precursor, Se-powder and sodium borohydride acts as selenium source as a reducing agent and using DMF (N, N-dimethylformamide) as solvent. Further, the surface morphology, crystal structure and optical properties, were investigated using Scanning & Tunnelling electron microscopy, X-ray diffraction, photoluminescence, UV–visible and Raman spectroscopies.

CHAPTER – 1

Introduction

1.1 Two-Dimensional (2D) Materials

Atomically thin two-dimensional (2D) materials have thicknesses of a few nanometers or less and electrons in these materials can move freely in two dimensions, but their motion is restricted motion in third dimensions due to quantum mechanics [1]. Such examples include quantum wells, graphene etc. They are crystalline materials made up of single- or few-layer atoms with much stronger in-plane interatomic interactions than those along the stacking direction. Due to their unique structures and remarkable properties, 2D materials have captivated the world's attention since the first exfoliation of single-layer graphene. In comparison to existing materials, graphene, which is composed of hexagonally arranged sp^2 hybridized atoms, has extraordinary strength, massive carrier mobility, extremely high thermal conductivity, and excellent optical properties[1]. Graphene's exceptional properties and single-atomic-layer structure allow it to be used in a wide variety of field-effect transistor (FETs), photodetectors, flexible electronics composite materials, storage of energy precise sensors. Semiconducting TMDC materials (MoS_2, WSe_2, WS_2, $SnSe_2$, etc.) have a tunable bandgap (1.2 eV to 2.5 eV), making them appealing for optoelectronics applications. Because of its tunable bandgap, 2D materials have emerging applications in electronics industry like sensing, spintronics, plasmonic, photodetectors, ultrafast lasers, batteries, supercapacitors, and thermoelectric.

1.2 Transition Metal Dichalcogenides (TMDCs) Materials

TMDCs are semiconducting 2D materials, and is made up of two elements: one transition metal atom (M) and one chalcogen atom (X). The chemical formula for TMDC material is MX_2, where M denotes a transition metal from groups 4 to 10 of the periodic table and X denotes chalcogen elements from group 16[2]. The transition element is highlighted in violet on the periodic table shown in Fig: 1.1, while chalcogen elements are highlighted in brown yellow. Bulk TMDCs can be semiconductors like MoS_2, $MoSe_2$, WSe_2, WS_2, etc., semimetals like $TiSe_2$, insulators like HfS_2, or metals like TaS_2 and $TaSe_2$ etc. [3].

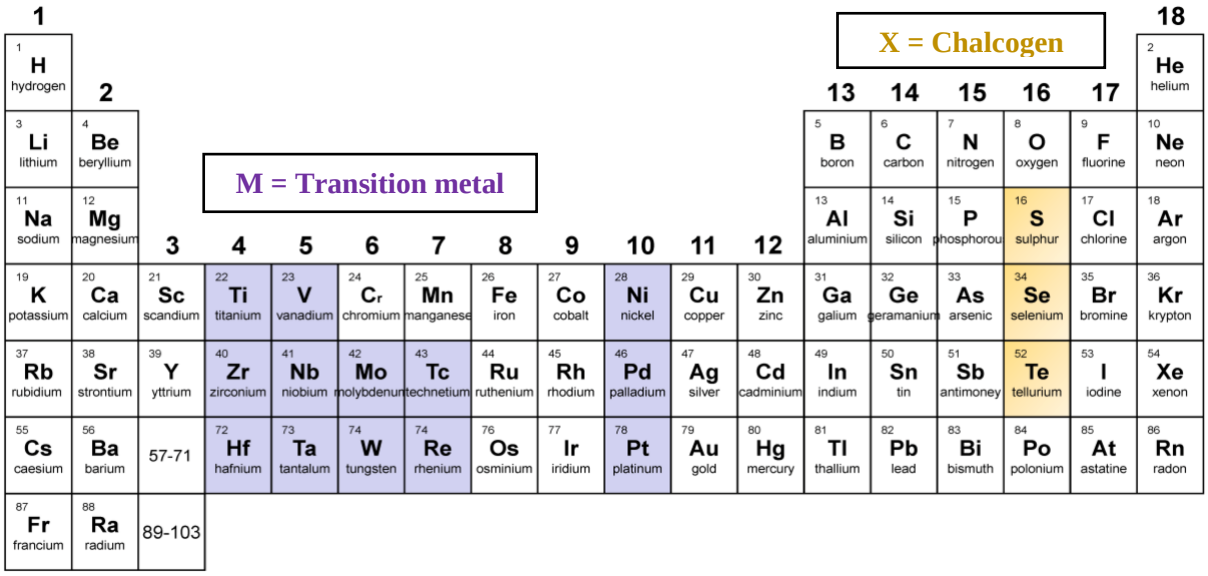

Fig 1.1 Periodic table of elements presenting the possible element combinations forming layered TMDCs MX_2[4].

While group 8–10 transition metals do not typically have a layered structure, TMDC materials containing group 4–7 transition elements frequently do. Three atomic layers make up the X-M-X unit layer, one of which is a center atom layer which is denoted as M positioned in the middle of two chalcogen atom layers denoted as X. TMDCs are found in layered structures resembling graphite[5]. In order to create single layers from bulk materials, such as through exfoliation, weak van der Waals forces stack the interlayers. The one-T, two-H, three-R, and Td phases are the most typical polymorphic crystal structures in TMDCs. Bulk TMDCs can be semiconductors such as $MoSe_2$, WSe_2, MoS_2, and WS_2 and metals such as VSe_2 and TiS_2 [6] superconductors such as TaS_2 and NbS_2, semimetals such as WTe_2 and $MoTe_2$ [6]. They have unique structural features and intriguing properties which is very useful in optoelectronics, electronics, mechanical, optical, catalytical, energy storage, applications. One of the most important factors that affect the properties and applications of 2D materials is the bandgap. For example, graphene is a semimetal with a no bandgap, which limits its applications to electronics and photonics. TMDCs have variable bandgaps that range from 0 to 3 eV and can be tuned by thickness, defects, dopants, and mechanical deformations. MoS_2, $MoSe_2$, WS_2, and WSe_2 are some of the semiconducting TMDCs that have been the subject of the most studies [7]. With increasing thickness, the bandgap widens and changes from being indirect in bulk crystals to being direct in monolayers[8].

1.3 Tungsten disulfide and Tungsten diselenide Properties

The chemical formula of Tungsten disulfide and Tungsten diselenide is WS_2 and WSe_2 respectively. It is member of the group of TMDC materials. Tungsten is a period 5 part and sulphur and selenium is a period 3 part.

1.3.1 Crystal Structure:

The electronic band gap of tungsten disulfide (WS_2) shifts from indirect (1.4 eV) to direct (2 eV) when its size is reduced from bulk to single layer. The nanosheets of WS_2 can be used for a variety of applications, including fluorescent emitters and field effect transistors [9], as well as photovoltaics and photocatalysis, in single layer form. There have only been a few reports of colloidal syntheses to our knowledge, and they rarely discuss the optical properties of the synthesized nanosheets. The majority of the attention had been focused on semiconducting WS_2 and MoS_2 single layers, both of which have prismatic coordination for the metal atom which has 2-Hexagonal structure. This type of structure is commonly created through vapor growth or physical exfoliation methods. Using the lithium exfoliation technique, it is possible to obtain a different structure with octahedral coordination which has 1-Trigonal structure for the metal atom. The 1-Trigonal structure describes the metallic properties. These 1Trigonal-WS_2 and 1Trigonal-MoS_2 single layers have recently been shown to be highly efficient hydrogen evolution electro-catalysts[10]. Fig.1.2 shows two single crystals of hexagonal structure of WX_2 (X = S, Se) drawn by Quantum ATK software. In this, figure have one Tungsten (W) atom in blue colour and two disulfide/diselenide (S/Se) atoms in yellow colour

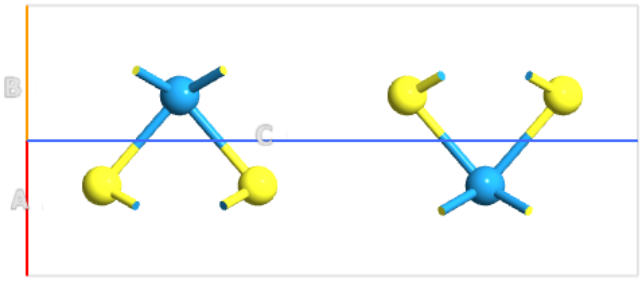

Fig: 1.2: Two single crystal of WX_2 (X = S, Se) (TMDC materials)

Fig.1.2 Schematic atomic structure of two single crystals of hexagonal structure of WX_2 (X = S, Se) drawn by Quantum ATK software.

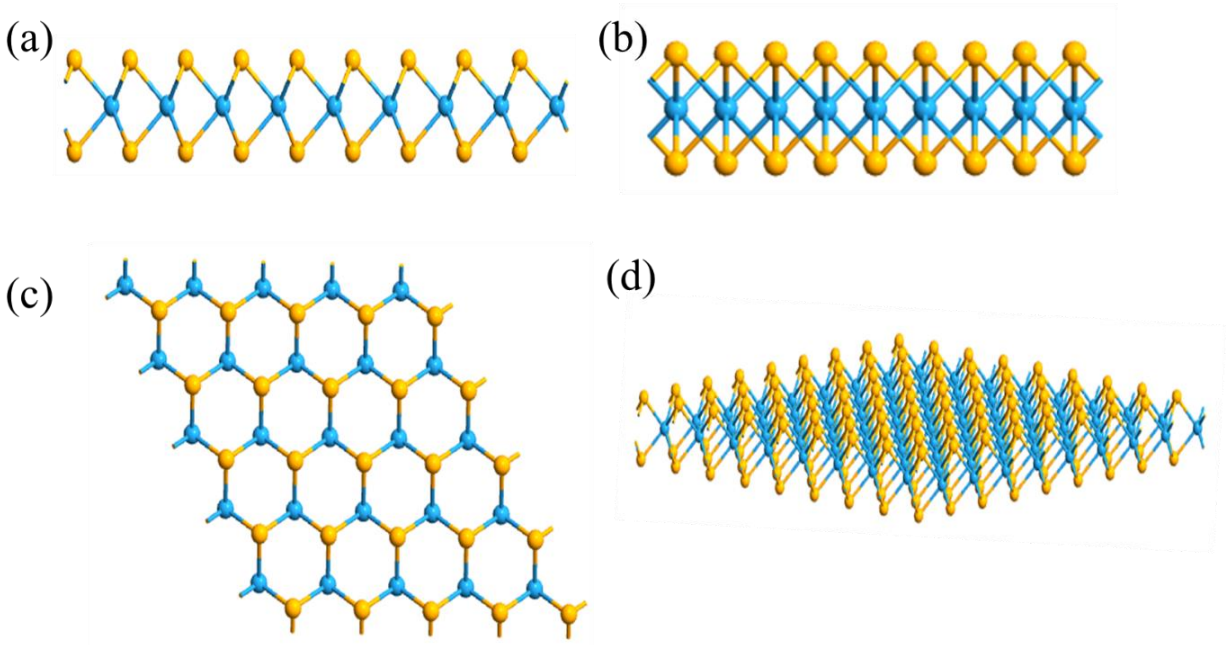

Fig.1.3 (a)-(d) Shows that the layered structure of WX_2 monolayer and bilayer (in 2D and 3D) structure

1.3.2 Band Structure:

WSe_2 and WS_2 are tungsten-based dichalcogenides. These are the members of the same layered transition metal dichalcogenide (LTMD) family as MoS_2 [11]. Recently, it was demonstrated that WSe_2 and WS_2 atomically thin sheets those are mechanically exfoliated had electrostatic modulation of conductance and high in-plane carrier mobility, similar to MoS_2[19]. Both substances are bulk indirect gap semiconductors with a bandgap of 1–1.3 eV [12] [3]. The length of the M-M bond (where M represents a transition metal atom) is nearly identical for WS_2 (3.15 Å) and MoS_2 (3.16 Å), but slightly longer for WSe_2 (3.28 Å)[12]. Because of the large Se atoms, the interlayer distance is proportionally larger for WSe_2. The general characteristics of the WSe_2 and WS_2 band structures are similar to those of MoS_2, in that a indirect gap and direct coexist regardless of thickness. A direct gap exists between the spin–orbit split valence band and the doubly degenerate conduction band at the Brillouin zone's K points [13]. In contrast, an indirect gap forms between the Γ point's valence band maximum and a local conduction band minimum at a midpoint between Γ and K. Because of the different sizes of the transition metal atoms, the primary difference between MoX_2 and WX_2 is the size of the spin–orbit splitting [12]. The band gap of TMDC materials varies for different materials, for example, direct band gaps of monolayer of MoS_2, $MoSe_2$, WS_2, and WSe_2, are estimated to be 1.88 eV, 1.57 eV, 2.03 eV, 1.67 eV respectively, whereas the indirect band gaps are 1.23 eV,

1.09 eV, 1.32 eV, and 1.21 eV respectively [14-21]. Here, in this work the band structure of WS_2 and WSe_2 materials has been simulated by using Quantum ATK software (https://www.synopsys.com/silicon/quantumatk.html).

The band structures of the bulk, monolayer and bilayer of WSe_2 and WS_2 layers are analyzed by the density functional theory (DFT) using the Quantum ATK. In this DFT calculation, we have used a numerical Linear Combination of Atomic Orbitals (LCAO). In the LDA calculations, we use k-point meshes of 14 × 14 × 7, 14 × 14 × 3, 14 × 14 × 14 and 14 × 14 × 14 have been used in bulk monolayer, bilayer respectively [22-24].Using the DFT-LDA calculations. Fig: 1.4 and 1.5 shows that the band structures of bulk, monolayer and bilayer of WSe_2 and WS_2 calculated at the DFT level. The green dotted lines in horizontal indicate the Fermi level. The black-colored arrows indicate the fundamental band gap i.e., it may be direct or indirect for a given system. The base of the conduction band and peak of valence band are highlighted in black, blue and red colour for bulk, monolayer and bilayer respectively. Then we show that poly layers of WSe_2 and WS_2 are indirect band gap semiconductors. The fundamental band gap initiates from transition from the base of conduction band halfway between Γ and K points while the peak of valence band situated at Γ point. The optical direct band gap is situated at K point. As the number of layers decreases, the fundamental band gap increases that is why band gap is high in the monolayer and material changes into a 2D indirect to direct band gap semiconductor. The band gap (Eg) of WSe_2 for bulk 1.1 eV, monolayer 1.55 eV [25] and for bilayer 1.17 eV. The simulated band structures of WSe_2 are shown in the Fig.1.4. (a), (b) and (c). The band gap (Eg) of WS_2 for bulk 0.97 eV, monolayer 1.79 eV and for bilayer 1.14 eV. The simulated band structures of WS_2 are shown in the Fig.1 4. (a), (b) and (c).

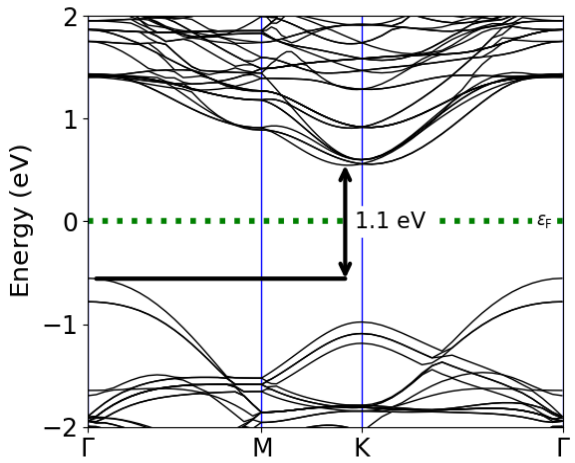

(a)

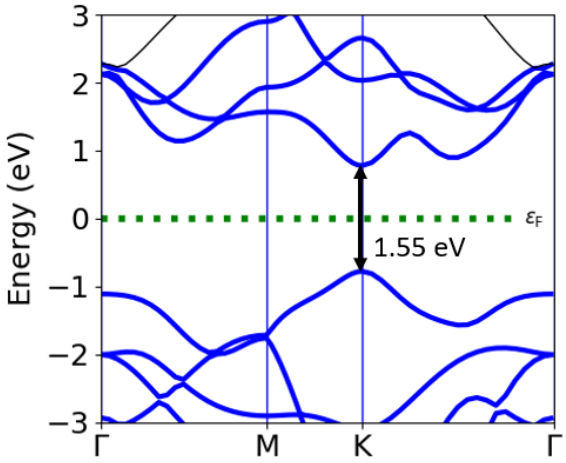

(b)

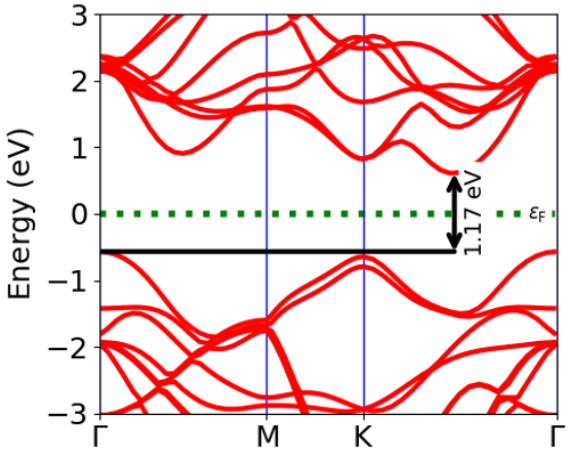

(c)

Fig.1.4: Band Structure of WSe_2 (a) Bulk (b) Monolayer (c) Bi-layer, simulated by using Quantum ATK. The solid light green line represents Fermi Level. The arrows indicate the fundamental band gap i.e. direct band gap or indirect band gap for a given system.

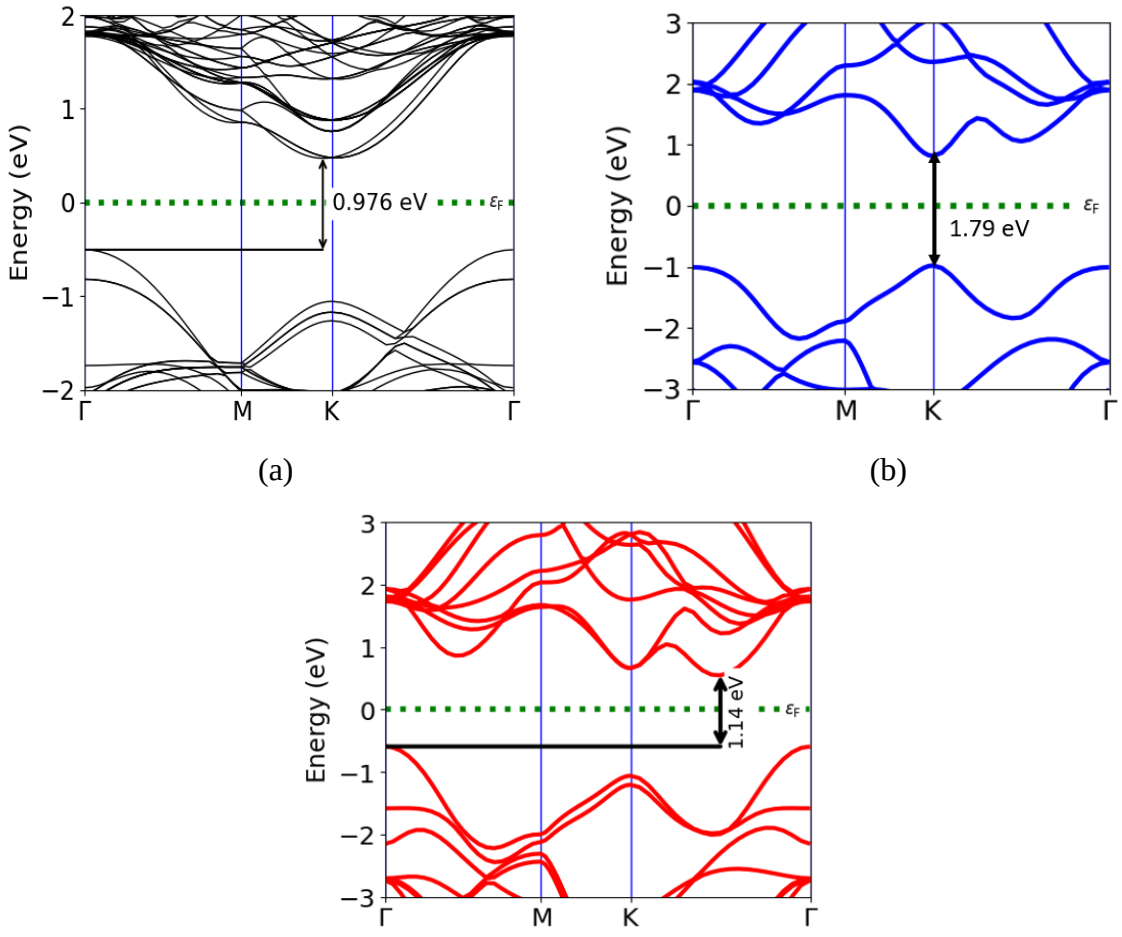

Fig.1.5: Band Structure of WS_2 (a) Bulk (b) Monolayer (c) Bi-layer, simulated by using Quantum ATK. The solid light green line represents Fermi Level. The arrows indicate the fundamental band gap i.e., direct band gap or indirect band gap for a given system.

This bulk material has also been demonstrated to be useful in a variety of applications, including hydrogen evolution reaction catalysts and photovoltaic devices. Indeed, the properties of TMDs such as MoS_2, WS_2, and WSe_2 have been reported to be directly related to the number of layers in the structure, particularly few layers[12, 26]. Monolayer WSe_2 also has a small band-gap (smaller than monolayer MoS_2) and shows ambipolar transport. Several potential optoelectronic applications, such as LEDs, photodetectors, solar-energy convertors and transistors, have been described using monolayer WSe_2. The appealing reported properties and potential applications of WSe_2 materials necessitate a well-controlled synthesis, including the number of layers, crystallographic phase composition, or/and film morphology[12, 26].

1.4 Quantum Confinement

The term "quantum confinement" refers primarily to the energy of confined electrons (electrons or electron hole). When comparing bulk materials to nanocrystals, the energy levels of electrons will not be continuous. Furthermore, when the confined electron wave functions are obtained, they become a discrete set of energy levels. These effects, which lead to energy changes or discrete levels, happen when the potential's dimensions get close to the "de Broglie wavelength of electrons". Due to the phenomenon, which is referred to as quantum confinement, nanocrystals are frequently called "quantum dots"[27]. The electrical, optical, and mechanical properties of nanomaterials are also impacted by the quantum confinement effect [27]. Because of their unique properties, nanomaterials have higher energy electrons than bulk materials. Depending on the size of the QD, confined electrons have higher energy than electrons in bulk materials. Interesting properties emerge when the dimensionality of semiconductor nanomaterials is reduced from 2D to 1D or 1Dto 0D. When the size and shape of nanomaterials are reduced to less than 100–10 nm or even less, the quantum confinement effect may occur. The changes caused by the discrete set of electron energy levels result in size confinement. To learn more about quantum confinement, first understand the phenomenon of QDs. QDs are a new type of material with quantum confinement effects. QDs are nanometer-sized semiconductor crystals, and molecules are 3D tightly confined electrons or electron–hole pairs known as excitons. QDs are a subatomic group in the family of nanomaterials, which also includes semiconductors, metals, insulators and other organic materials. Because semiconductor QDs have a tunable bandgap as opposed to metals, quantum confinement occurs only in semiconductor QDs. As previously stated, materials with the unusual tunable band gap properties QD are only found in groups II–VI, III–V, and IV–VI. Because the bandgap,

electrical and optical properties are tunable in response to particle size changes, they have a wide range of applications. The diagram below depicts energy band structures in atoms, bulk materials, and quantum nanostructures.

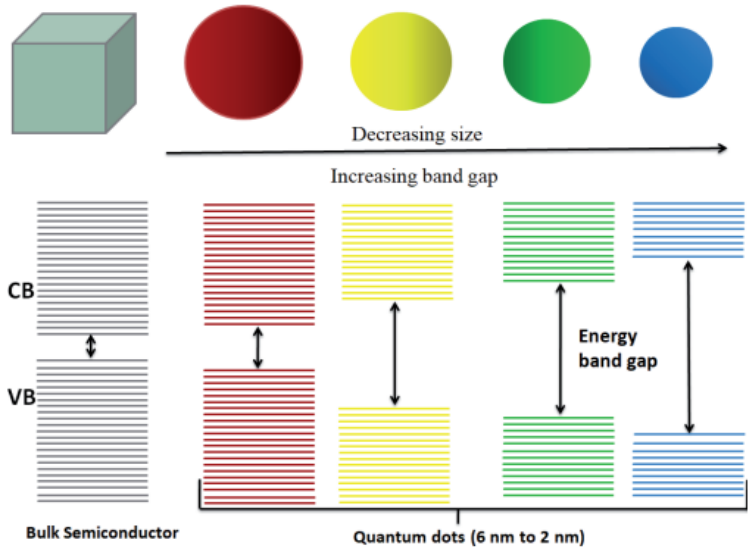

Fig. 1.6 Schematic diagram showing energy band structures in atom, bulk material, and quantum nanostructure[27].

When atoms are carried together in a bulk material, the number of energy state increases, forming nearly continuous state bands, which helps to explain the formation of discrete energy levels. Furthermore, due to confinement, the number of atoms in the material decreased, and energy states were delocalized. When particles in the conduction band start moving toward the natural de-Broglie wavelength of electrons, the phenomenon generates electron-hole pairs and a spatially confined nature. As a result, as particle size decreases, the energy difference between energy bands increases[28].

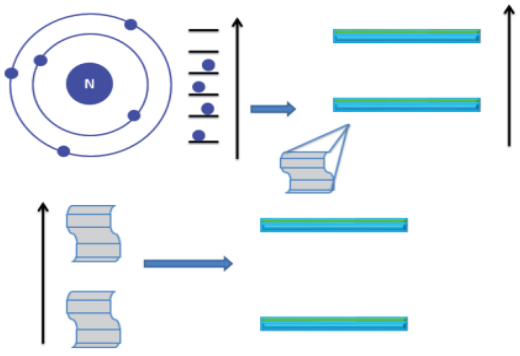

Fig.1.7 Schematic diagram for the formation of discrete energy levels[27].

The particle behaves like a free particle when the dimensions of the confining structure are very large in comparison to the de Broglie wavelength. When the confining structure's dimensions are reduced to the nanometer scale, the energy states turn continuous and the bandgap restored to its original position, whereas another energy spectrum doesn't remain continuous and thus becomes discrete in nature. Due to these size-dependent characteristics, the bandgap eventually results in a blue shift in the emitted light as particle size decreases. Contrastingly, this effect illustrates what happens when you restrict the number of electrons and electron-hole pairs also known as excitons to a dimension that approaches the critical quantum limit, also known as the "Bohr Radius". The equation of the Bohr radius is

$$a_B = \varepsilon \frac{m_0}{m^*} a_0 \qquad (1.1)$$

Where, m* = mass of the particle, ε = dielectric constant of the material, a_0 = Bohr radius of the hydrogen atom, and m_0 = rest mass of electron. When the particle size approaches the Bohr radius, the exciton causes the energy of the exciton transition to increase [29]. Furthermore, quantum confinement causes the continuous energy zones of bulk material to be broken down into discrete atomic approximating energy levels. The discrete absorption spectrum of energy states is depicted in Fig. 1.7. The motion of the carriers, namely electron - hole pairs, is constrained in all directions by potential barriers in a quantum bounded structure [29]. A quantum bounded structure is classified into three categories based on the direction of confinement: quantum well, quantum wire, and quantum dots or nanocrystals[29]. According to Table.1.1, this is the most common type of quantum bounded structure.

Table 1.1: Classification of Quantum Confined Structures

Structure	Quantum Confinement	No. of Dimensions
Bulk	0	3
Quantum well	1	2
Quantum wire	2	1
Quantum dot	3	0

1.4.1 Particle in Quantum Confined Structure

In QDs due to quantum-confined structure their properties fall somewhere between bulk semiconductors and discrete molecules. The size effects are common in semiconductor nanoparticles with dimensions of 10–100 nanometers, whereas quantum size effects are more common in nano crystallites with dimensions of less than 10 nanometers. There are two reasons why the physicochemical characteristics of nanocrystalline particles are different from those of bulk materials. First of all, the high surface-to-volume ratio causes a lot of atoms to be at the crystalline lattice's surface. Second, due to the charge carriers' confinement, the electronic bands are divided into discrete energy levels. The bandgap increases with decreasing particle size due to quantum confinement of charge. As the semiconductor particle radius shrinks to a size comparable to or smaller than the exciton radius, the bandgap, (Eg) increases in magnitude[30]. These characteristics have led to applications in a variety of fields, including super lattice devices, semiconducting quantum well, nonlinear optical materials and imaging systems and photocatalysis. Dabbousi *et al.*[31] determined the maximum radii for the onset of Q-size effects leading to bandgap increase for II–VI compounds to be 10 to 100 Å. It is obvious that QCE-based semiconductor nanocrystals were produced with far superior electrical properties and optical than bulk materials, owing to the reduced behavior of characteristic length known as exciton "Bohr diameter". When a material exhibits size-dependent optical and electrical properties, the characteristic length is usually in the range of a few nanometers[27]. Quantum confinement occurs when the location of a particle (for example, holes and electrons) is confined to a region of space. This is the concept underlying the "Particle in a Box" system. When visualized as area of space, the walls of a one-dimensional box fill with an infinitely large potential energy. On the other hand, if it comes into contact with the box's walls, the infinitely large forces repel the particle. The potential energy in this model is given as

$$\boldsymbol{V(x)} = \begin{cases} \mathbf{0}, \mathbf{0} < \boldsymbol{x} < \boldsymbol{L} \\ \infty, \boldsymbol{otherwise} \end{cases} \qquad (1.2)$$

Where $\boldsymbol{x}$ is the position within the box and L is the length.

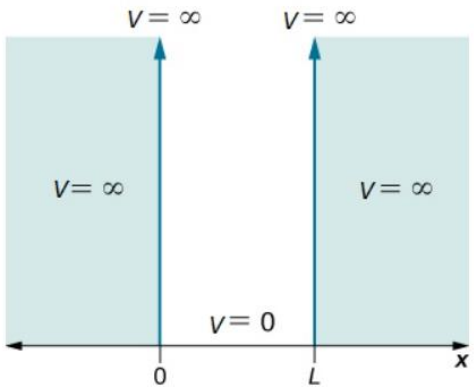

Since the particle would have an infinite potential energy if it were discovered there, which is obviously impossible, the infinite potential energy acts as an impenetrable barrier. Wave function is the most fundamental description of a particle's behavior in quantum mechanics. The wave function can be determined by solving the Schrödinger equation for the system, which is written as

$$\boldsymbol{\psi(x,t) = [A\,sin(\,kx) + B\,cos(\,kx)]e^{-iwt}} \qquad (1.3)$$

By applying boundary conditions, we get

$$\boldsymbol{\psi(0) = \psi(L) = 0} \qquad (1.4)$$

$$\boldsymbol{\psi(x) = \sqrt{2/L}\,sin(\frac{n\pi x}{L})} \qquad (1.5)$$

The energy quantum number or principal quantum number is denoted by the index n. The first excited state is the one for n = 2, the second excited state is the one for n = 3, and so on. The first three quantum states (for n=1,2,3) of a particle in a box shown in below figure:

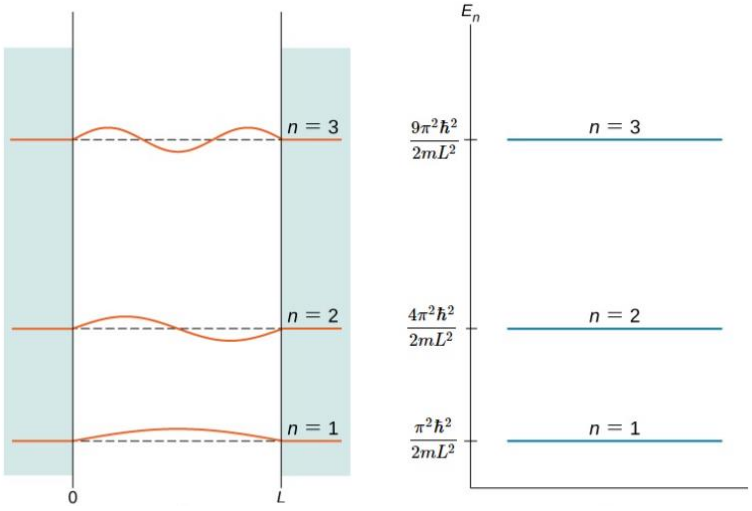

We know for the free particle, when V(x) =0, we get

$$\boldsymbol{E\psi(x) = \frac{-\hbar^2}{2m}\frac{d^2}{dx^2}\Psi(x)} \quad (1.6)$$

After the calculation we get,

$$\boldsymbol{E_n = \frac{n^2\hbar^2}{8mL^2}} \quad (1.7)$$

Due to quantum confinement, the quantum dot's radius affects the wavelength of the light that is emitted. Because E = hc/λ, where c is the speed of light, this effect of a change in the quantum dot's radius on the wavelength of the emitted light is described by this equation. This is useful for calculating the radius of a quantum dot using experimentally determined parameters. So, the general equation is as follows:

$$\boldsymbol{\Delta E(r) = E_{gap} + \frac{h^2}{8r^2}(1/m_e^* + 1/m_h^*)} \quad (1.8)$$

Where, r is the radius of quantum dots, m_e^* and m_h^* are effective mass of electron and hole respectively, E_{gap} is the energy gap of the band.

1.5 Synthesis Process for 2-D TMDC Materials

Several methods for synthesizing 2-D materials have been proposed. 2D material synthetic routes can be divided into two categories: (a) top-down methods and (b) bottom-up methods. Top-down methods determine the formation of 2D nanostructures by isolating one or a few atomic layers from the bulk using external energy Bottom-up methods, on the other hand, are processes in which atoms are deposited on a substrate through thermal or chemical reactions to create 2-D nanostructures. The most common methods for creating 2D nanostructures are chemical exfoliation, micromechanical exfoliation, solvothermal synthesis, and chemical vapor deposition. Other techniques for creating 2D nanostructures have been proposed, such as, laser thinning, carbothermal reduction and laser ablation [5].This section will discuss about the different synthesis processes for 2D nanostructures.

1.5.1 Micromechanical Exfoliation:

Geim and Novoselov discovered the micro-mechanical exfoliation (MME) process in 2004 [32], and single layer graphene was achieved by removing the bulk material with the micromechanical force of scotch tape and placing it on top of the photoresist [33]. This cleavage is possible because of the weak interlayer van der Waals forces[5]. Scotch tape is used in this process to exfoliate an atomic layer thick graphene from bulk graphite mesas, which is then deposited on the substrate. Apart from graphene, this process has produced single layers of, MoS_2[34], and WS_2[35] and $NbSe_2$[36]. Micromechanical exfoliation, despite its speed and low cost, is not suitable for industrial-scale production of single layer materials because the most of the flakes are smaller than 20 meter in diameter. The monolayer formed by this process, on the other hand, is highly crystalline and retains its structural integrity due to the lack of chemical interaction. This monolayer remained stable at room temperature for months[5, 36].

1.5.2 Liquid Exfoliation:

In comparison to mechanical exfoliation, which produces low yields, liquid exfoliation can produce mono or few layers of 2D materials on a large scale. This method can easily produce mono or few layers of Bi_2Te_3, $TaSe_2$, $MoSe_2$, $MoTe_2$, BN, WS_2, and MoS_2 [8, 37]. This method is classified into four types: intercalation, oxidation, ultrasonic cleavage and ion exchange. By treating graphite flakes with potassium chlorate, potassium permanganate, sulfuric acid, nitric acid, or a mixture of these acids, graphene oxide can be created via oxidation[38]. The process of adding and dispersing epoxide functional groups or –OH in a polar solvent, followed by sonication, results in exfoliated graphene oxide. This method is also referred to as the Hummers method or the modified Hummer method[39]. For layered materials with low reduction potential, an oxidative form of liquid exfoliation is preferable. The intercalation of ionic or organic molecules reduces interlayer force in this technique, which lowers the energy needed for exfoliation[40]. Ultrasonic cleavage is another method for obtaining a single- or few-layered 2D material via liquid exfoliation. The bulk material, which consists of layers with weak interlayer bonding, is ultrasonically treated for one to three hours after dispersion in a suitable solvent. Cavitation bubbles are formed in the solvent as a result of high-energy ultrasonic waves in this process [41]. The pressure released by the burst of cavitation bubbles allows for layer exfoliation. The crystals are then separated using centrifugation.

1.5.3 Chemical Vapor Deposition (CVD):

The bottom-up technique of Chemical Vapor Deposition makes it possible to synthesize uniformly thick 2D layers on a large scale, making it a promising candidate for optoelectronic and electronic devices. One of the most recent developments is the CVD synthesis of MoS_2 2D nanostructured sheets on an oxidized silicon substrate. In general, there are two methods for producing monolayer 2D materials. Taking Molybdenum disulfide as an example, a bottom-up, two-step e-beam evaporation process evaporates a thin layer of metallic Molybdenum. Sulfur vapors, which are created by heating elemental sulfur above its melting point, then react with the Molybdenum layer. This reaction takes place at 750 °C and creates monolayered MoS_2.[42] Second, the atomically thick MoS_2 nanosheets are synthesized using a one-step bottom-up technique. This method involves adding pure S and MoO3 powders to a CVD system. 650 degrees Celsius are applied to the mixture. On the Si substrate, which is covered in rGO (reduced graphene oxide) for the growth of MoS_2 layers, the atomic layer of MoS2 will then be grown. In order to encourage the formation of MoS_2 layers, the rGO serves as both a catalyst and a seed[43]. Furthermore, large-area MoS_2 nanostructured sheets can be obtained by dip coating silicon or silicon dioxide substrate with $(NH_4)_2MoS_4$ (ammonium thiomolybdate) dissolved in DMF (dimethylformamide). After the $(NH_4)_2MoS_4$ solution is dipped onto the substrate, it is annealed for 1 hour at 500 °C in an Ar/H_2 atmosphere. The substrate is then subjected to a second annealing at 1000 °C for 30 minutes in an Ar or Ar^+S atmosphere[44]. Other 2D materials produced using CVD techniques include TiS_2[45], VSe_2[46], WSe_2[47], WS_2[48], and $MoSe_2$[49].

1.5.4 Hydrothermal Synthesis

A substance crystallizes using the hydrothermal method when exposed to high vapor pressure and temperatures and an organic or aqueous solution. This method can only be used with precursors that can resist the extreme conditions because of them. In a liquid medium, it is a form of bottom-up synthesis. Hydrothermal synthesis is defined as a process that takes place in water. In essence, these wet chemical techniques use chemical reactions and substrate deposition to create 2-D nanostructures. Chemical synthesis is an economical and scalable synthesis method for 2-D TMDC materials. The ideal stoichiometry in the finished product is, however, relatively challenging to achieve when a TMDC is chemically synthesized. This method has been used to successfully synthesize 2D layered nanostructured materials. Single-layered $MoSe_2$ and MoS_2 nanostructures were created by chemically reacting Se/S with $(NH_4)6Mo_7O_{24}4H_2O$ (ammonium molybdite) in hydrazine monohydrate solution for 48 hours

at 150–180 °C[50]. Other 2D materials have also been produced using the hydrothermal method, in addition to the synthesis of MoS_2 mono and a few layered 2D nanostructures. In oleyl amine, metal chloride was used to create 2D nanostructures of transition metal chalcogenides (groups IV and V) [51]. Chalcogen sources such as elemental sulfur, selenium used in this process. When sulfur is used as the source, TMDC has poor crystallinity and irregular shape owing to the highly reactive radical formation.

1.6 Characterization Method for 2-D TMDC Materials

Spectroscopy techniques have been around for a long time and have been widely used for many years in the chemical, biological, and engineering fields. Many spectroscopy methods can now be used to characterize nanomaterials, as nanotechnology has evolved into its own distinct field. Some were derived from general chemistry, while others came about naturally as a result of measuring inorganic complexes and are now applied to nanomaterials. In this study, we look at some of the most popular and successful spectroscopy techniques for describing nanomaterials. Nanomaterials, as well as other materials and molecules, are often characterized using spectroscopy techniques. To give a complete picture of the nanomaterial under consideration, they are frequently used in combination with different microscopy techniques. While spectroscopy offers a wealth of knowledge about a nanomaterial's chemical structure and properties, microscopy techniques are used to image nanomaterials and provide a pictorial representation.

1.6.1 Transmission Electron Microscopy (TEM):

The microscopy technique known as transmission electron microscopy (TEM) involves passing an electron beam through a very thin specimen while it interacts with it[52]. An image is created by the interaction of electrons that are transmitted through the specimen and then magnified and focused onto an imaging device. Recent studies of pharmaceutical compounds have demonstrated that not only can these challenges be overcome, but also that TEM analysis can provide a variety of useful information. Although TEM has been less frequently used in the study of organic materials due to perceived difficulties with sample preparation and beam damage Because it can magnify a tiny particle as small as 2 nanometers, its resolution is limited to 0.2 μm. Operating similarly to a light microscope is the Transmission Electron Microscope (TEM). The main difference is that TEMs produce images by focusing an electron beam on the specimen, whereas light microscopes focus light rays to create an image. Compared to light,

which has a long wavelength, electrons have a shorter wavelength. They can be used in a variety of fields due to the high-resolution power they generate, which enables their working mechanism. There are three working parts that includes the electron gun, image producing system and image recording system. The electron beams are generated in the first section of the Transmission Electron Microscope. A cathode, which is a V-shaped tungsten filament that is normally heated, creates electrons. The cathode can be found either above or below the cylindrical hole. The cathode and control grid are both negatively charged, as is the disk-shaped end of the anode, which also has an axial hole. The objective lens, as well as projector lenses and intermediate, comprise the second section of the TEM. They function by focusing electrons as they pass through the specimen, producing a highly magnified image. Electrons are allowed to pass through a fluorescent screen that is affixed to the base of the microscope in order to create an image that is visible to the human eye. The image can also be captured digitally and displayed on a computer before being saved in JPEG or TIFF format. Fig. 1. 8 shows that schematic diagram of TEM System.

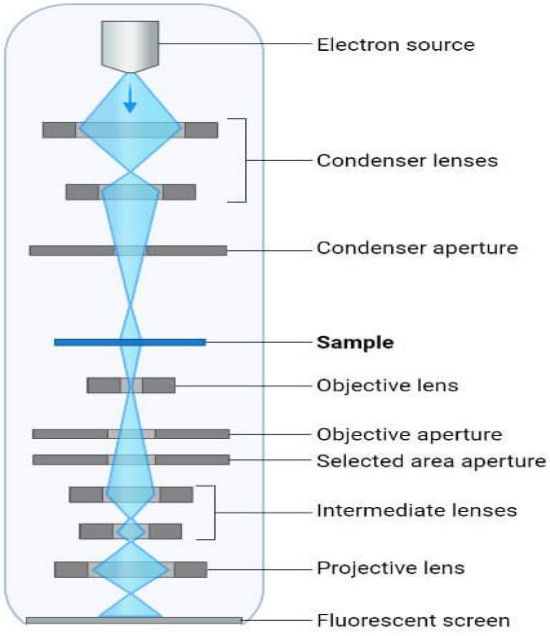

Fig. 1.8 Schematic diagram of Transmission Electron Microscopy (TEM) [52]

1.6.2 Scanning Electron Microscopy (SEM):

By projecting a focused stream of electrons across a surface, a scanning electron microscope (SEM) produces an image. The interaction between the beam's electrons and the sample results in a variety of signals that can be used to infer information about the surface's topography and chemical composition. Most often, a small portion of the sample's surface is used to gather data, which is then used to create a 2-dimensional image that shows how these properties vary spatially. Areas with widths between 1 cm and 5 microns can be imaged in scanning mode using standard SEM techniques. Additionally, the SEM is able to analyze particular point locations on the sample; this technique is particularly helpful for figuring out crystalline structure, crystal orientations, and chemical compositions[53]. The following are the main SEM components that includes, electromagnetic lenses, electron generator, electron detector, sample chamber and display to view the images. The sample is set up on a stage in the chamber area, and a number of pumps are used to evacuate both the chamber and the column. The position of the electron beam on the sample is managed by scan coils that are located above the objective lens. This beam gathers data about a particular region of the sample. Images are created by scanning the sample with a higher energy electron beam in a scanning electron microscope. The interaction of the electrons with the sample results in backscattered electrons, secondary electrons, and differentiated X-rays. These signals are gathered by more than one detectors to create images, which are then shown on the computer screen[53] . Fig. 1. 9 shows that schematic diagram of SEM System.

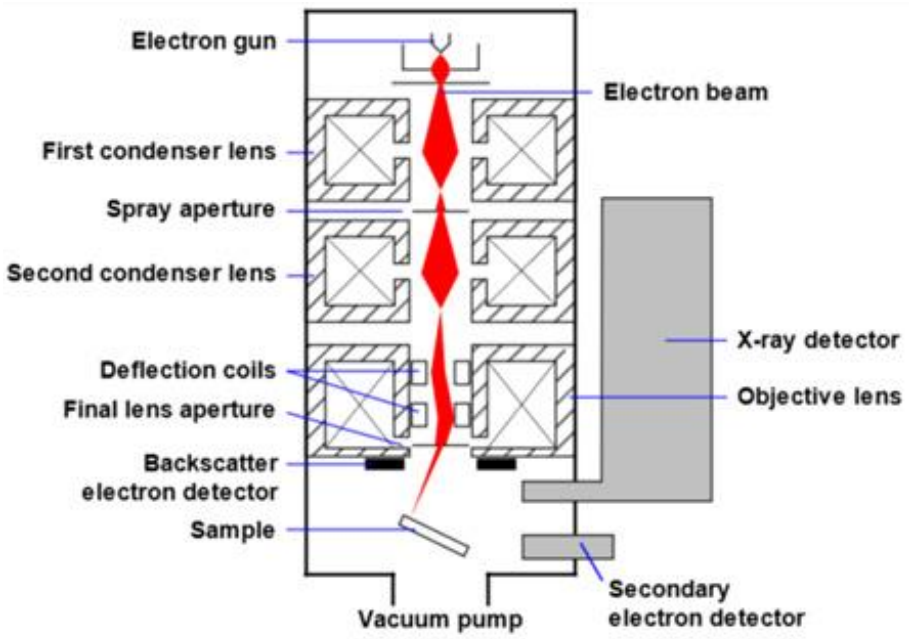

Fig. 1.9 Structure of Scanning Electron Microscopy[53]

1.6.3 Atomic Force Microscopy (AFM):

Atomic force microscopy is used in laboratories to obtain images with atomic resolutions of one tenth of a nanometer. AFM system components include a micro-cantilever motion detection device, micro-cantilever with probe, a feedback process for monitoring the motion, a sample scanning device made up of piezoelectric ceramic, and a display processor. Fig. 1. 10 shows that schematic diagram of AFM System. It detects very weak interatomic interactions between the sample surface and the probe tip to study the surface structure and properties of the sample. The basic idea behind how it works is to resolve one end of a cantilever, which is highly sensitive to weak force, while enclosing the other end in the probe and bringing it in close contact with the sample [54]. After that, a very weak force—which may be either attractive or repulsive—exists between the atoms of the sample surface and the probe's tip. The magnitude of this force alters the deformation or motion state of the micro cantilever. In order to obtain surface information in nanometer resolution, sensors detect these changes and gather force distribution data when the sample is scanned. The X, Y, and Z directions are available for the AFM scanner to move in. The vertical Z direction is typically constrained to a few microns, while the X and Y directions vary depending on the scanner. Restoring the position of the piezo - electric scanning tube in the three-dimension planes allows one to simultaneously determine the morphology of the scanning area sample. A smaller Young's modulus indicates that the sample is more prone to deformation. The force between the tip and the sample is

depicted experimentally in the force-distance curve of atomic force microscopy. AFM can quantify the elastic modulus, adhesion, and hardness of a material by measuring the nano-indentation of micro regions using respective probes outfitted with specialized software [55] [56].

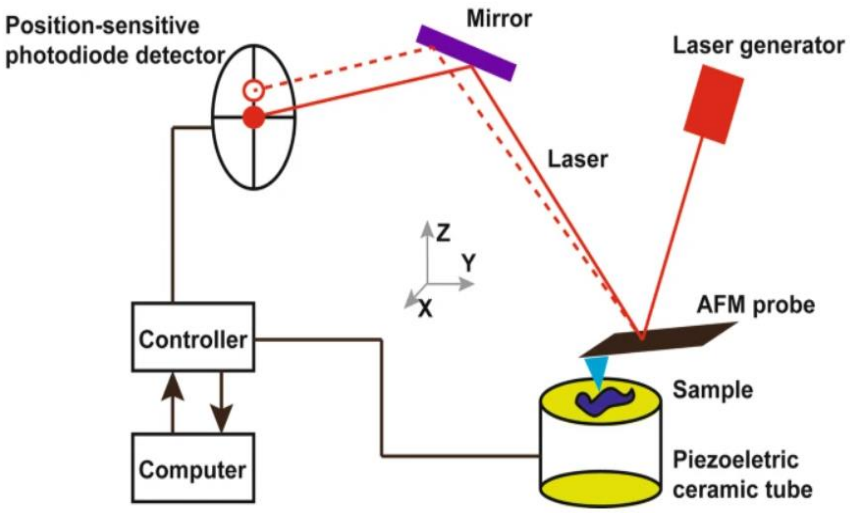

Fig. 1.10 AFM working principles are depicted schematically[56]

The attraction and repulsive forces between atoms are at the heart of AFM imaging and mechanical property detection. An attractive force acts when atoms at the probe's tip and those on the sample's surface are too far apart, and a repulsive force act when they are too close. Contact mode, non-contact mode, and tapping or semi-contact mode are the three basic imaging modes of AFM. When in contact mode, the atomic force microscopy probe keeps a minimal amount of force and contact with the sample surface. By measuring the atomic attraction between the probe and the sample, the surface topography of the sample is created in the non-contact mode. In the tapping mode, the cantilever of the probe is compelled to move close to the resonance frequency and makes scattered contact with the sample. Controlling amplitude or deflection of the micro-cantilever when the probe touches the sample allows the force between the probes and sample to be kept constant[56]. Fig. 1.11 shows different three basic working modes of an AFM.

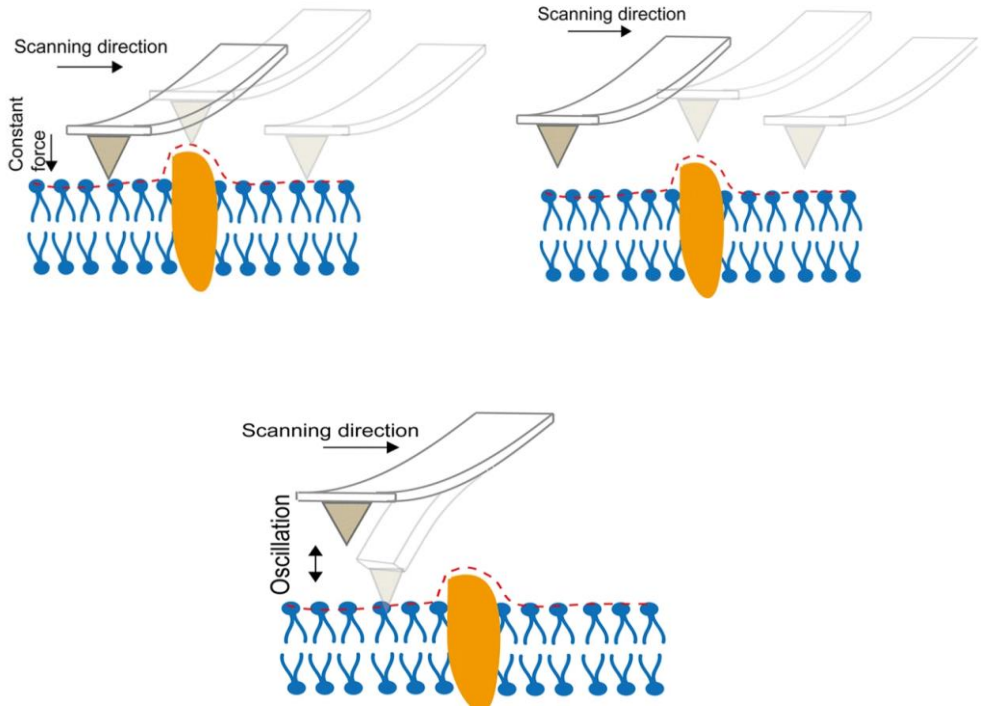

Fig. 1.11 Three basic working modes of AFM. (a) Contact mode of AFM. (b) Non-contact mode of AFM (c) Tapping mode of AFM [56].

1.6.4 X-ray Diffraction:

The crystallinity of a material is observed by using the X-ray diffraction (XRD) method in materials research. When using XRD, a material is subjected to incident X-rays, and the emitted X-rays intensities and backscattered angles are then measured[57]. Identification of materials based on their diffraction pattern is a primary application of XRD analysis. In addition to phase characterization, X - ray diffraction analysis gives details on how defects and internal stresses cause the actual structure to deviate from the ideal structure [57]. Fig.1.12 shows that schematic diagram of explaining Braggs Law. Max von Laue discovered in 1912 that crystalline materials function as 3D diffraction gratings for X-ray wavelengths because their plane spacing is similar to that of a crystal lattice. On the constructive interference of monochrome X-rays and a crystals sample, X-ray diffraction is based. These X-rays are generated by a cathode ray tube, filtered to create monochromatic radiation, concentrated by collimation, and then directed at the sample. If all of the conditions are met, Bragg's Law i.e. $n\lambda = 2d \sin \theta$ states that the incident rays interact with the sample to produce constructive interference (and a diffracted ray)[57].

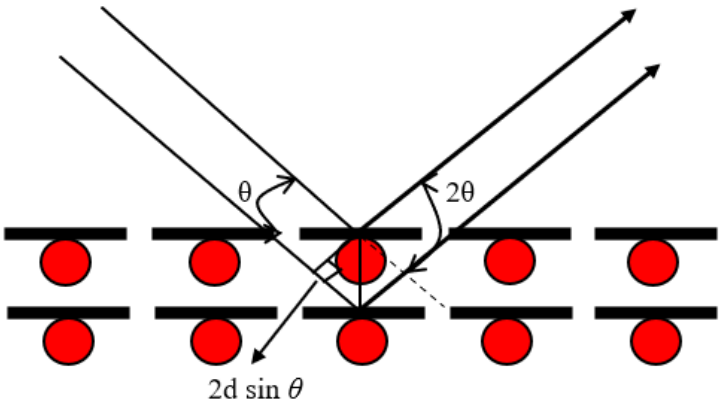

Fig. 1.12 Bragg's Law

This law explains how the diffracted angle and lattice spacing in a crystal sample relate to the wavelength of electromagnetic radiation. The X-rays that have been diffracted are then found and examined. The sample should be scanned through a variety of 2θ angles in order to obtain all possible scattering directions of the lattice due to the powdered material's random orientation. Normally, this is done by comparing the d-spacings to accept reference patterns. The production of X-rays in an X-ray tube is a basic requirement for all diffraction techniques. The diffracted rays are collected after the X-rays are directed at the sample. The angle between the incident and diffracted rays are crucial factor in all types of diffraction. A sample holder, an X-ray tube, and an X-ray detector are three fundamental parts of an X-ray diffractometer. By heating a filament to create electrons, accelerating the electrons with a voltage toward a target, and then bombarding the target material with the electrons, a cathode ray tube can create X-rays. Characteristic X-ray spectra are created when electrons have enough energy to knock out inner shell electrons in the target material. Before being directed at the sample, these X-rays are collimated. As the sample and detector are rotated, the strength of the reflected X-rays is measured. This X-ray signal is captured and processed by a detector which gives outputs as a count rate to a gadget like printer or computer monitor. The geometry of an X-ray diffractometer is such that the sample rotates at an angle θ in the path of the collimated X-ray beam and the X-ray detector rotates at an angle of 2θ while being mounted on an arm to collect the diffracted X-rays. The tool used to hold the angle and rotate the sample is called a goniometer. For typical powder patterns, data is gathered at 2 angles which are predefined X-ray scan angles ranging from 10° to 60°[58].

1.6.5 UV-Vis Spectroscopy:

In UV - vis spectroscopy, which is a type of absorption spectroscopy, a molecule absorbs light in the ultra-violet range (200–400 nanometer), which excites electrons from their ground state to a higher energy state[59]. Fig. 1.13 block diagram of UV-Vis Spectroscopy includes a light source, monochromator, sample and reference cells, detector and data output. The energy difference between the two states is referred to as the band gap. In order for a photon to be absorbed, its energy must be equal to the band gap. Beer's Law governs the principle of absorption. Spectroscopy is concerned with the interaction of light with matter. When light is absorbed by matter, the energy content of the atoms or molecules increases. When UV radiations are absorbed, electrons are excited from their ground state and moved to a higher energy state. Molecules with -electrons or nonbonding electrons (n-electrons) can absorb ultraviolet light energy to excite these electrons to higher anti-bonding molecular orbitals. Longer the wavelength of light that electrons can absorb, the easier it is to excite them. Transitions are classified into four types such as π–π*, σ–σ*, n–π*, and n–σ* and they are ordered as: σ–σ* > n–σ* > π–π*> n–π* [59]. When a chemical compound absorbs UV light, it produces a distinct spectrum that aids in compound identification. UV-Vis spectroscopy is a technique for comparing the amount of discrete wavelengths of visible light or UV absorbed or transmitted through a blank sample. This property is impacted by composition of the sample and may reveal information about what is in the sample and at what concentration. Measuring instruments and UV spectrometer operation can be considered, and the most recent modern UV spectrometers include a light source, monochromator, sample and reference cells, detector, amplifier, and recording devices [60].

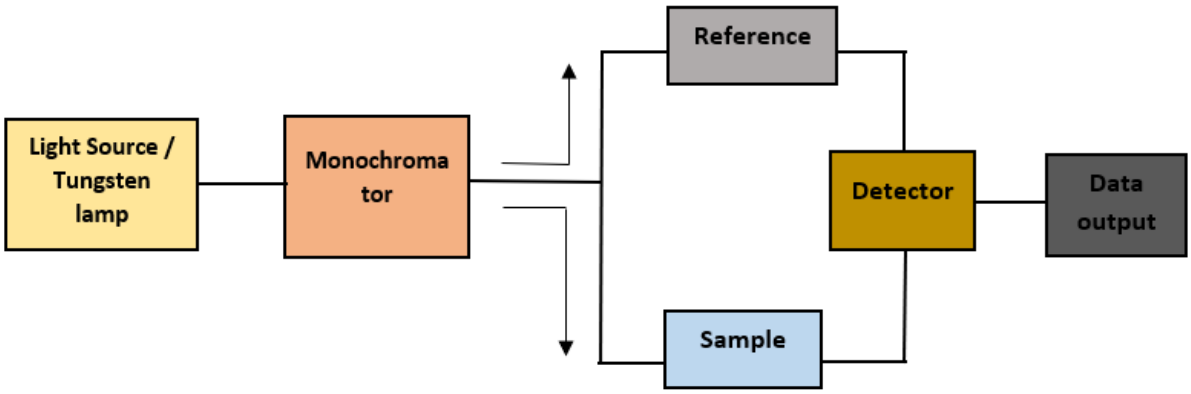

Fig. 1.13 Block diagram of UV-Vis Spectroscopy includes a light source, monochromator, sample and reference cells, detector and data output

1.6.6 Photoluminescence (PL) Spectroscopy

Photoluminescence spectroscopy is a nondestructive, contactless process of analyzing the electronic structure of materials. Beam of light is focused onto a specimen called sample, where it is absorbed and transmits extra energy into the material, in a process known as photo-excitation. The sample can dissipate extra energy by emitting light, which is known as luminescence. This luminescence is known as PL in the case of photo-excitation. Electrons within a material move into permissible excited states as a result of photo-excitation. These excited electrons dissipate the extra energy through a radiative process, which is the emission of light, or through a non-radiative process to reach their equilibrium or ground state, which is stable. The energy difference between the two electronic states involved in the transition between the excited and equilibrium states is correlated with the energy of the light that is emitted. In contrast, the proportion of the radiative process determines the amount of light emitted. Fig. 1.14 shows schematic diagram of PL process[61, 62].

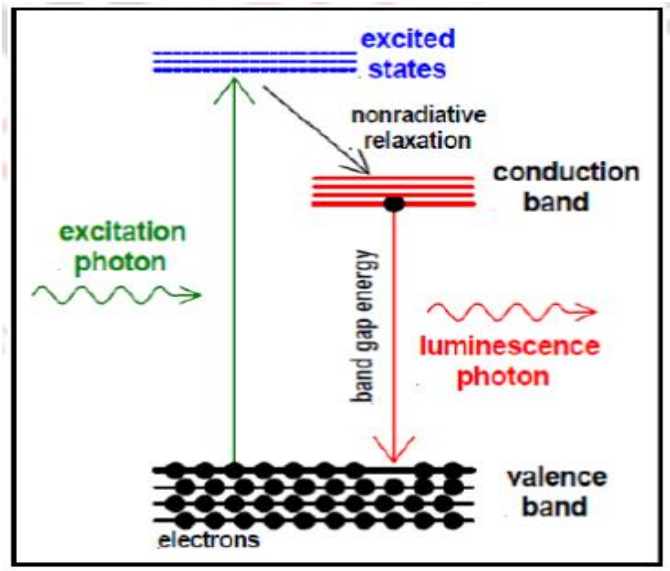

Fig. 1.14 Structural diagram of photoluminescence spectroscopy (PL)[63]

A spectrofluorometer is an analytical device that records and measures the fluorescence of a sample. To record the fluorescence, the excitation, emission, or both wavelengths are scanned. The study of signal deviation with respect to time, temperature, concentration, polarization, or other variables is observed using extra attachments. Figure 1.15 depicts a block diagram of a fluorescence spectrometer. Fluorescence spectrometers use monochromators (wavelength selectors), laser sources (sample illumination), detectors, and corrected spectrum[63].

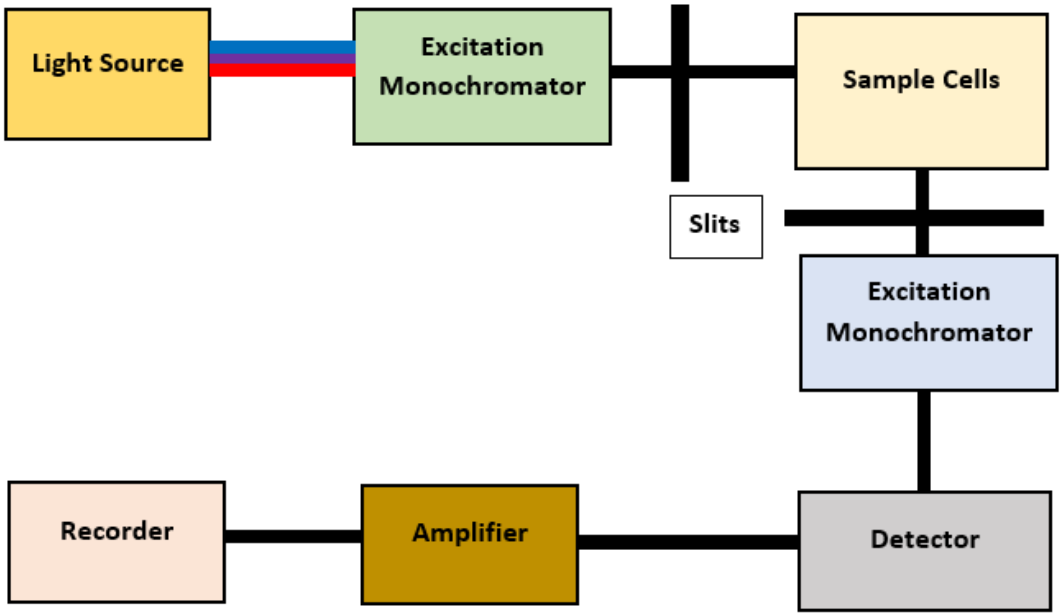

Fig. 1.15 The block diagram of photoluminescence spectroscopy.

1.6.7 Raman Spectroscopy

Detailed information about chemical structure, crystallinity, phase, polymorph, and molecular interactions can be obtained using the non-destructive chemical analysis technique known as Raman spectroscopy. It is predicated on how light interacts with chemical bonds in a substance. The Raman effect, discovered in 1928 by Indian physicist Chandrasekhara Venkata Raman, is the foundation of Raman spectroscopy. The Raman effect is based on light scattering, which includes Raman scattering also known as inelastic at different wavelengths brought on by molecular vibrations as well as Rayleigh scattering also known as s elastic at the same wavelength as the incident light[64]. Rayleigh scattering is one million times less intense than Raman scattering. Rayleigh scattering must therefore be kept from overwhelming the weaker Raman scattering in order to obtain Raman spectra. When a sample is excited by a powerful laser beam, the scattered light is then run through a spectrometer to produce a Raman spectrum [64]. Fig.1.16 shows working principle of Raman spectroscopy.

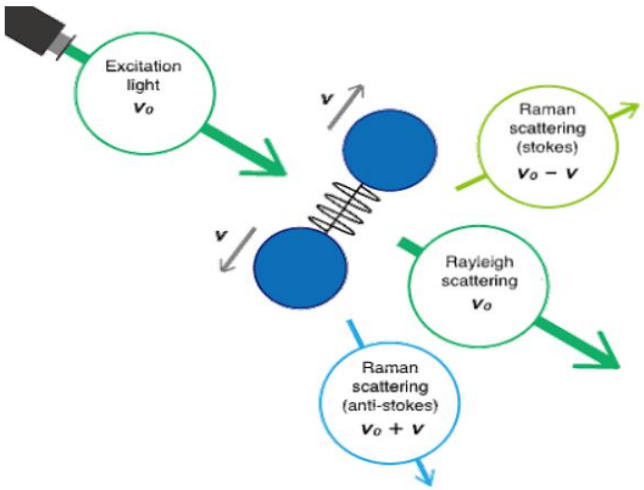

Fig. 1.16 Molecular vibrations and Raman scattering[65]

The scattering intensity is represented by the vertical axis in the resulting spectrum, and the Raman shift wavenumber (cm^{-1}) is represented by the horizontal axis. Two distinct energy bands are associated with the Raman shift. The shift at wavelengths longer than those of the incident light is referred to as Stokes scattering. The shift that occurs at wavelengths that are shorter than the incident light's is known as anti-Stokes scattering. With an excitation wavelength of 532 nm, Figure 1.17 displays the Raman spectrum of sulphur (green laser). Anti-Stokes peaks can be used in addition to higher intensity Stokes scattering peaks for analysis[65].

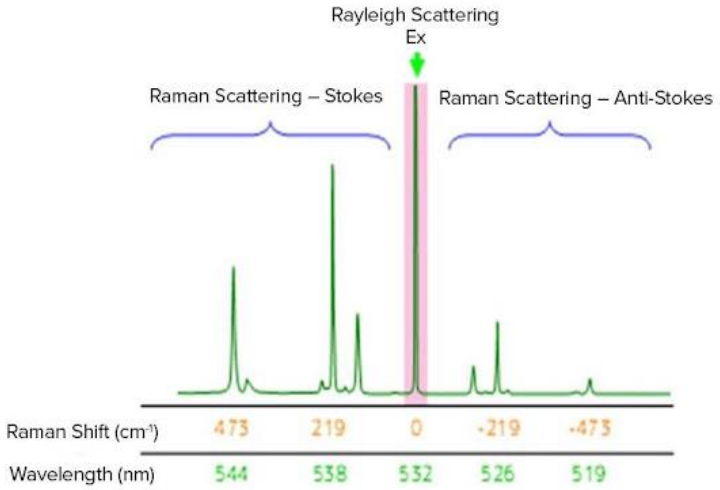

Fig. 1.17 Raman Scattering diagram of Raman Spectroscopy[65]

1.7 Motivation of Thesis:

2D materials are gaining popularity due to their unique potential benefits for a wide range of optoelectronic devices. TMDCs are among the most appealing 2D layered materials for photodetector applications because of their unique band structures and excellent electronic properties. TMDC 2D monolayers have direct band gaps, whereas bulk structures have indirect band gaps. They have promising electronic and optical properties that make them suitable for photodetector applications. When 2D WS_2 materials are reduced to zero or low dimensions, new optical properties emerge. As a result, it suggests a lot of potential technological advantages in electronic, optical, and catalytic properties. Because of its simple synthesis route and high electrical charge mobility with n-type charge transport, MoS_2 is one of the most studied members of the TMDC family. The advancement of semiconducting TMDC materials has shed light on both conventional semiconductor physics, such as photodetectors, transistors, and light-emitting diodes. Most TMDCs are n-type semiconductors, and a few are p-type, for example, WSe_2. However, because WSe_2 is more difficult to synthesize as compare than MoS_2, it is not fully understood. Therefore, the main motivation of present thesis is to synthesis n-WS_2 QDs and p-WSe_2 NSs on p-Si/n-Si and ITO substrates for multifunctional optoelectronic devices applications.

CHAPTER – 2

Literature Review

2.1 Introduction:

Two-dimensional (2D) materials have received a lot of attention in recent years, with the introduction of nanosheets and ultrathin films. In comparison to their three-dimensional (3D) bulk counterparts, their often superior electrical, optical, and mechanical properties offer a promising field of opportunities. By downsizing and improving materials at the same time, new research fields for existing and novel applications are opened. Supercapacitors, electrochromic devices, (bio-)chemical sensors, photovoltaic devices, thermos electrics, (photo-)catalysts, and membranes are among the most promising application fields. Two-dimensional quantum dots have also attracted a lot of attention in recent years due to their intriguing properties and widespread use in photodetectors, sensors, batteries, white LEDs, phototransistors, and other devices. Researchers are intrigued by the unique optical and electronic properties of thin films two-dimensional quantum dots derived from layered transition metal dichalcogenide, graphene and phosphorene[66]. Layered transition metal dichalcogenides MX_2, have piqued the interest of researchers due to their distinct optical, electronic and chemical properties. M is a transition metal (such as W, Mo, and Nb) and X is a chalcogen (Se, S, and Te). Many different applications, including, batteries, photocatalysis, electrocatalysis and electronic devices have been thoroughly researched for WSe_2 and WS_2. A W atomic layer is sandwiched between two hexagonal chalcogen atomic layers in the layered structure of WSe_2 and WS_2, which is Se–W–Se or S–W–S. Weak van der Waals forces connect the interlayers, and the intralayer W–Se/S bonding is covalent.

2.2 Literature Review:

In 2014, Hai Li *et. al.* demonstrated *"Preparation and Applications of Mechanically Exfoliated Single-Layer and Multilayer MoS_2 and WSe_2 Nanosheets".* In this paper, the author described the preparation, characterization, and applications of mechanically exfoliated 1L and multilayer MoS_2 and WSe_2 nanosheets. In order to distinguish between single-layer and

multilayer MoS_2 and WSe_2 nanosheets on a Silicon substrate encapsulated with 90 and 300 nm SiO_2 during the nanosheet preparation, the author proposed a straightforward optical identification method. Furthermore, Raman spectroscopy was used to characterize mechanically exfoliated 1L and multilayer WSe_2 nanosheets. In 2017, Xinqiang Wang *et. al.* demonstrated *"Graphene-like WSe_2 nanosheets for efficient and stable hydrogen evolution".* In this paper, author reported simple, low cost, and one-pot solvothermal synthesis of graphene-like few-layered WSe_2 nanosheets for the design of effective catalysts for electrochemical hydrogen evolution. The prepared WSe- NSs were characterized by transmission electron microscopy (TEM), Scanning Electron Microscopy (SEM), X-ray Diffraction (XRD), and Raman Spectroscopy. In 2018, Bing-Qian Zhang *et. al.* demonstrated *"Synthesis of ultrathin WSe_2 nanosheets and their high-performance catalysis for conversion of amines to imines"*. In this paper, author reported simple colloidal method for synthesis of WSe_2 nanosheets. The prepared WSe_2-NSs were characterized by atomic force microscopy (AFM), transmission electron microscopy (TEM), X-ray Diffraction (XRD), X-ray photoelectron spectroscopy, and Raman Spectroscopy, UV–vis spectroscopy as well as, photoluminescence spectroscopy (PL). The samples size, composition, morphology, valence as well as other characteristics were analyzed quantitatively. The obtained WSe_2 nanosheets, which had a thickness of 0.7 nm, had strong blue fluorescence, according to the results. In 2020, Ayrton Sierra-Castillo *et. al.* demonstrated *"Synthesis and Characterization of Highly Crystalline Vertically Aligned WSe_2 Nanosheets".* In this article, author reported quick selenization of thin tungsten films in an atmospheric pressure chemical vapor deposition method for the synthesis of tungsten diselenide (WSe_2) nanosheets. Electron microscopy, UV–vis spectra, Raman and photoluminescence spectroscopies, and X-ray diffraction and X-ray photoelectron spectroscopy were used to examine the morphology, structure as well as its optical characteristics of the material. The high crystallinity, purity, orientation and quality of the WSe_2 nanosheets were confirmed by these research as well as the unexpected presence of mixed phases in addition to the most stable crystalline 2H phase. The material created could be useful in applications such as hydrogen evolution reaction catalysis or gas sensing. In 2021, Pengshang Zhou *et. al.* demonstrated *"Synthesis of Colloidal WSe_2 Nanocrystals: Polymorphism Control by Precursor-Ligand Chemistry".* In this article author described synthesis of WSe_2 nanosheets with oleylamine and 1T′ phase-dominated nanoflowers with oleic acid. The morphology and structure of the material, as well as its optical properties, were investigated using electron microscopy, and Raman spectroscopies, UV–visible and X-ray diffraction and X-ray photoelectron spectroscopy. In 2017, A. Bayat *et. al.* demonstrates

"Synthesis of blue photoluminescent WS_2 quantum dots via ultrasonic cavitation". In this work author reported straightforward top-down procedure that included tip ultrasonication, centrifugation in a water bath, and water-ethanol in 0.7:0.3 ratio as a friendly solvent was used to create blue photoluminescent WS_2 quantum dots (QDs). Bulk WS_2 flakes were broken down into quantum dots by cavitation at high power (300 W). Transmission electron microscopy, atomic force microscopy, X-ray diffraction UV–vis and photoluminescence spectrophotometry, were used to examine the synthesized WS_2 QDs. In 2018, Wenxu Yin *et. al.* demonstrates *"Rational Control of Size and Photoluminescence of WS_2 Quantum Dots for White Light-Emitting Diodes".* In this work author reported that by using a hot-injection methodology in a non-coordinating solvent, highly luminescent WS_2 quantum dots with controllable particle size were formed. The Bohr radius is even smaller than the particle sizes. The 32 percent photoluminescence quantum yield and narrow size distribution of the as-obtained WS_2 quantum dots are both remarkable. With a maximum brightness of 507 cd/m^2, colour temperatures that can be adjusted from 4100 K to 10,000 K, and a colour rendering index of 91, white light-emitting diodes were made using the WS2 quantum dot layer. The prepared WS_2-QDs were characterized by transmission electron microscopy (TEM), X-ray Diffraction (XRD), X-ray photoelectron spectroscopy, and UV–vis spectroscopy, photoluminescence spectroscopy (PL), and Raman Spectroscopy. In 2019, Da-Ren Hang *et. al.* demonstrates *"Facile Bottom-up Preparation of WS_2-Based Water-Soluble Quantum Dots as Luminescent Probes for Hydrogen Peroxide and Glucose"*. In this article, authors describe a Simple bottom-up approach for hydrothermal reaction using sodium tungstate dihydrate and L-cysteine as W and S sources to obtain higher water-soluble tungsten disulfide (WS_2) QDs. This method was also used to create hybrid carbon quantum dots/WS_2 QDs. The physicochemical and structural analysis of the QD hybrid revealed that electrostatic attraction forces held graphitic carbon quantum dots with diameters of about 5 nm to WS_2 QDs. The resulting QDs have good water solubility and photoluminescence stability (PL). The polydispersity of the synthesized QDs can be attributed to the excitation-dependent PL. The morphology and structure of the material, as well as its optical properties, were studied using atomic force microscopy (AFM), electron microscopy, UV–visible, photoluminescence, and Raman spectroscopies, and X-ray diffraction and X-ray photoelectron spectroscopy. In 2019, Vijay K. Singh *et. al.* demonstrates *"WS_2 Quantum Dot Graphene Nanocomposite Film for UV Photodetection"*. In this article, author outlined the fabrication of atomically thin UV photodetectors on a SiO_2/Si substrate using a hybrid structure (0D-2D) of semiconducting WS_2 quantum dots (0D) and graphene (2D). Chemical vapor deposition (CVD) and hydrothermal

processes are used to synthesise graphene and WS_2 quantum dots (WS_2-QDs). During hydrothermal synthesis, sodium tungstate dihydrate and L-cysteine were used as W and S sources. Graphene film was grown on 25μm thick Cu foil using the chemical vapor deposition (CVD) method and n-hexane as a liquid precursor for Chemical Vapor Deposition Synthesis (CVD). The morphology and structure of the material, as well as its optical properties, were studied using electron microscopy, atomic force microscopy (AFM), UV–visible and Raman spectroscopies. In 2020, Neema Pallikkarathodi Mani *et. al.* demonstrates *"Hydrothermal synthesis of WS_2 quantum dots and their application as a fluorescence sensor for the selective detection of 2,4,6-trinitrophenol"*. In this article, author outlined the quick and easy hydrothermal synthesis of WS_2 powder with NaOH to produce water-soluble fluorescent WS_2 QDs. The goal was to use fluorescence-based chemical sensing applications with WS_2-based nanomaterials. As a result, the synthetic parameters, such as temperature, time, and WS_2 to NaOH concentration ratio, were optimized to increase the PL quantum yield (QY). The prepared WS_2 Quantum Dots were characterized by atomic force microscopy (AFM), transmission electron microscopy (TEM), Raman Spectroscopy, and UV–vis spectroscopy, photoluminescence spectroscopy (PL) and X-ray photoelectron spectroscopy.

CHAPTER – 3

Synthesis of WSe_2 Nanosheets and WS_2 Quantum Dots on Si Substrates

3.1 Introduction

WS_2 and WSe_2 are 2D semiconductor material with distinct electronic and optoelectronic properties. According to the literature, both WS_2 and WSe_2 with small planar dimensions exhibits excitation dependent PL with wavelengths in the 300–600 nm range, which has numerous applications like optoelectronics, imaging, and sensors etc. As a result, high-quality and large-scale synthesis of WS_2 and WSe_2 nanostructures are required for the production of various electronic devices. It should be noted that when the size of WS_2 and WSe_2 reduced to less than 10 nm, the bandgap broadens further due to the effect of QCE, exhibits new size-dependent properties. Different top-down and bottom-up techniques for obtaining WS_2, and WSe_2 nanostructures have been reported in the literature; however, in this work, we simply create water-soluble WS_2 QDs using a bottom-up method. WSe_2 nanosheets through hydrothermal reaction.

3.2 Preparation of WSe_2 Nanosheets and WS_2 Quantum Dots by Hydrothermal Method

The advantages of hydrothermal methods include their simplicity and low energy requirements. Various TMDC materials have been successfully prepared using this method of preparation. N, N-dimethylformamide, which works with a reducing agent, sodium borohydride, and sodium tungstate dehydrate, to create WSe_2 films from selenium powder. A stainless-steel autoclave keeps the pressure high so that the reactions can take place over a quartz substrate. In this work, we easily create water-soluble WS_2 QDs using a bottom-up method. For the preparation of WS_2 QDs sodium tungstate dihydrate and L- cysteine as W and S sources.

3.3 Experimental Section

3.3.1 Chemical Required:

For WSe_2 Nanosheets synthesis, Se powder was obtained from Sigma-Aldrich © (-100 mesh, ≥ 99.5% trace metals), Sodium tungstate dihydrate ($Na_2WO_4 \cdot 2H_2O$) was obtained from EMPLURA® $Na_2WO_4 \cdot 2H_2O$, purity 99.0 percent. sodium borohydride was purchased from Alfa Aesar ($NaBH_4$, purity 95%). N, N dimethylformamide was obtained from EMPARTA® (anhydrous, purity 99.8%). They served as starting materials for the hydrothermal synthesis of WSe_2 NSs. Here, Se powder and Sodium borohydride acts as precursor and Sodium tungstate dihydrate as a reducing agent and N, N dimethylformamide as a solvent. Also, for WS_2 Quantum dots synthesis, Sodium tungstate dihydrate ($Na_2WO_4 \cdot 2H_2O$) was obtained from EMPLURA® $Na_2WO_4 \cdot 2H_2O$, purity 99.0 percent and L-cysteine was purchased from Alfa Aesar. Here, L-cysteine has served as sulfur source as well as reducing agent. Throughout the synthesis, DI water provided from laboratory and was adopted for solution preparation.

3.3.2 Synthesis of WSe_2 Nanosheets:

The WSe_2 nanosheets were prepared using a solvothermal method. 0.64 gm of Se powder, (powder -100 mesh, ≥ 99.5% trace metals, Sigma-Aldrich©), 0.20 gm of sodium borohydride, ($NaBH_4$, purity 95%, Alfa Aesar) and 1.32 gm of sodium tungstate dihydrate, ($Na_2WO_4 \cdot 2H_2O$, purity 99.0 percent, EMPLURA®) were dissolved in 60 ml of N, N Dimethylformamide (anhydrous, purity 99.8%, Sigma-Aldrich) and stirred continuously for about 2 hours. The mixture was placed in a 200 ml Teflon-lined stainless-steel autoclave and heated to 200-degree Celsius for 48 hours. Centrifugation was done to collect the black precipitates, which were then washed several times with distilled water and absolute ethanol. Following this step, a black colour precipitate was obtained and dried in an ice bath for 24 hours. Finally, the WSe_2 nanosheets were annealed at 400°C for 2 hours to improve their crystallinity. Lastly the final product was obtained and was stored in vacuum desiccator. The schematic diagram of synthesis of WSe_2 NSs is shown in Fig 3.1. The photo image of as-prepared WSe_2-NSs solution before annealing is shown in Fig. 3.2 (a), WSe_2 NSs powder after annealing at 200°C for 2 hrs shown in Fig. 3.2 (b), WSe_2 NSs solution dispersed in DI water for further use is shown in Fig. 3.2 (c), further the WSe_2 NSs under UV light to show the luminescence shown in Fig. 3.2 (d).

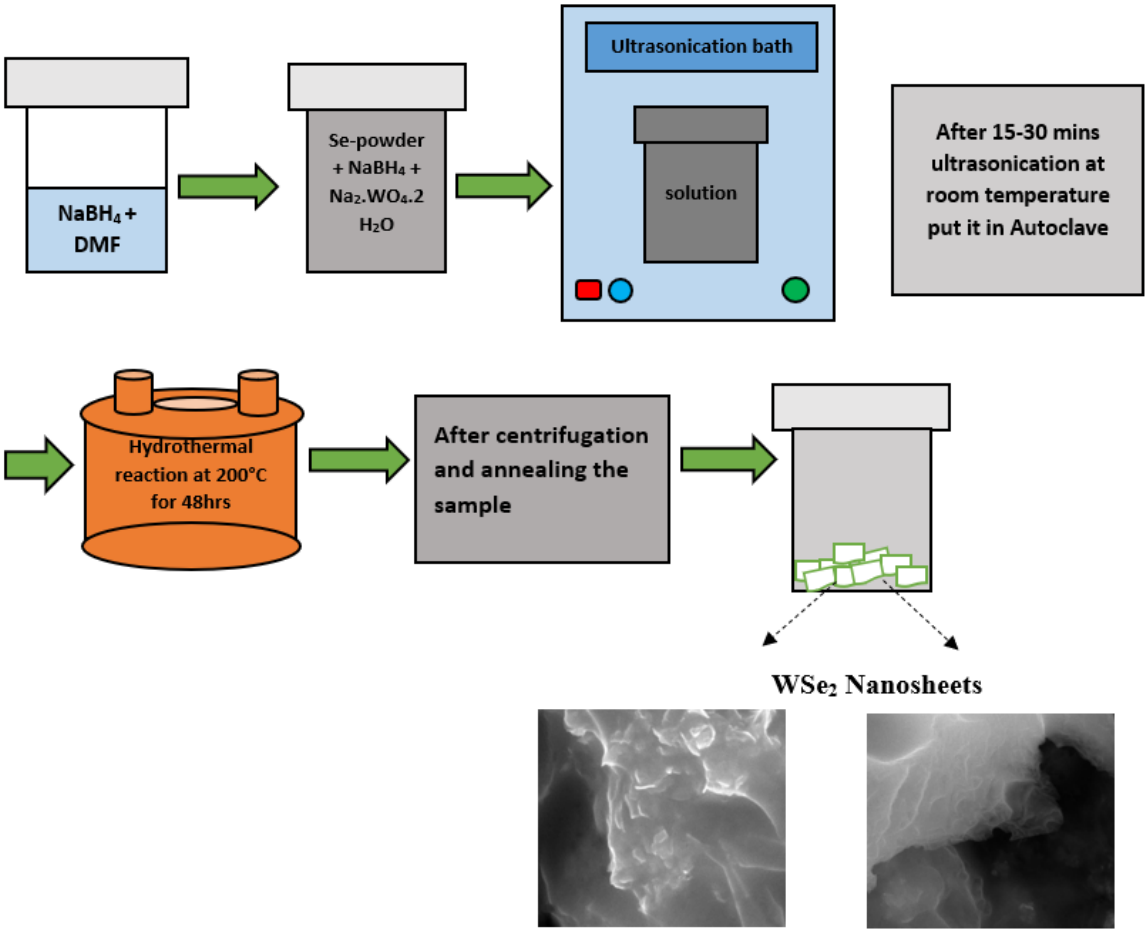

Fig: 3.1 Different steps of Colloidal synthesis process for WSe_2 Nanosheets: different forms of WSe_2 Nanosheets after every stage of synthesis are mentioned below.

- First image depicts the as prepared WSe_2 nanosheets before annealing followed by the powder formation after annealing at 200°C for 2 hrs.
- After that powder form of WSe_2 NSs was dispersed in DI water for further use.
- Last image depicts the photoluminescence of WSe_2 NSs under UV light.

(a) **(b)** **(c)** **(d)**

Fig: 3.2 (a) photo image of as-prepared WSe_2-NSs solution before annealing (b) WSe_2 NSs powder after annealing at 200°C for 2 hrs (c) WSe_2 NSs solution dispersed in DI water for further use. (d) WSe_2 NSs under UV light to show the luminescence.

3.3.3 Synthesis of WS_2 Quantum Dots

In this synthesis process, 0.25 g sodium tungstate ($Na_2WO_4 \cdot 2H_2O$) was dissolved in 25ml of DI water and stirred for 45 minutes. Simultaneously 0.5 g L-cysteine was dissolved in 50 mL DI water and stirred continuously for 45 minutes. Then the pH meter was calibrated with a buffer tablet at 7 pH level. Then after that 0.1M HCl solution was prepared by adding 0.9 ml of Conc. HCl to 99.1ml of DI water and the pH of that solution was calculated. Further both the above solution was uniformly mixed and pH of the solution was adjusted to 3 pH level by slowly adding 0.1M HCl solution dropwise. After 20-30 minutes of stirring, the solution was poured into stainless lined Teflon autoclave of 200 ml capacity and placed at oven for hydrothermal reaction. Initially the temperature was set to 120°C for 2.5 hours and then it was set to 190°C for 46 hours. After the reaction was completed, the oven was naturally cooled to room temperature, yielding a light yellowish colour solution containing WS_2-QDs. The obtained solution was then filtered in dialysis bag for 2-3 days. The schematic diagram of synthesis of WS_2 QDs is shown in Fig. 3.2. The photo image of as-prepared WS_2-QDs solution is shown in Fig. 3.4(a), the WS_2 QDs solution after filtration by dialysis bag for 2-3 days shown in Fig. 3.4(b), and the WS_2 QDs under UV light to show the luminescence shown in Fig. 3.4 (c).

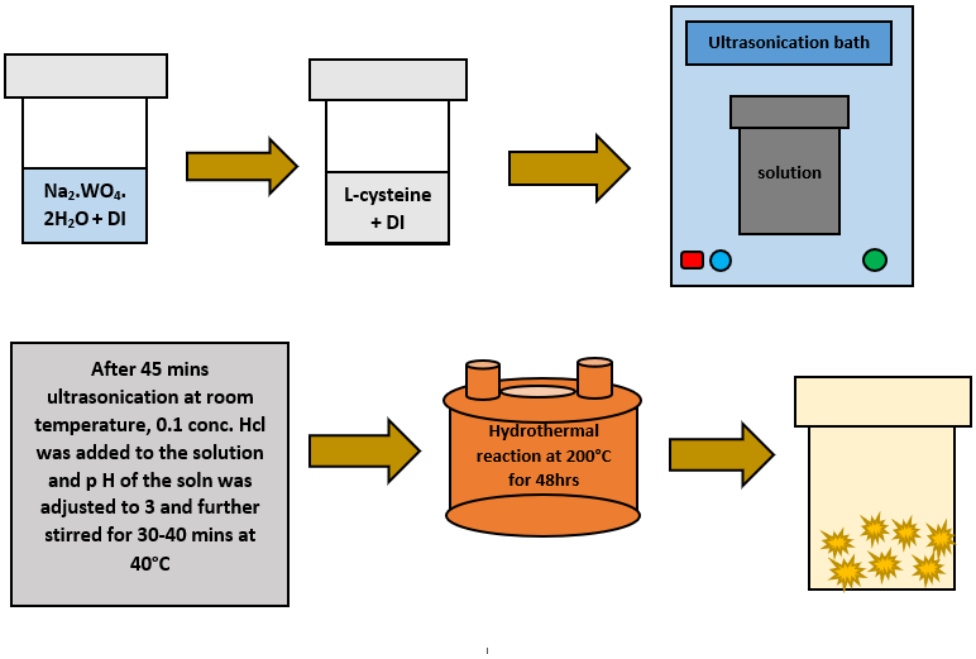

Fig. 3.3 Different steps of colloidal synthesis process for WS_2 Quantum dots

Different forms of WS_2 QDs after every stage of synthesis are mentioned below. First image depicts the as prepared WS_2 QDs in yellowish colour. After that WS_2 QDs was filtered in dialysis bag for 2-3 days. Last image depicts the photoluminescence of WS_2 QDs under UV light.

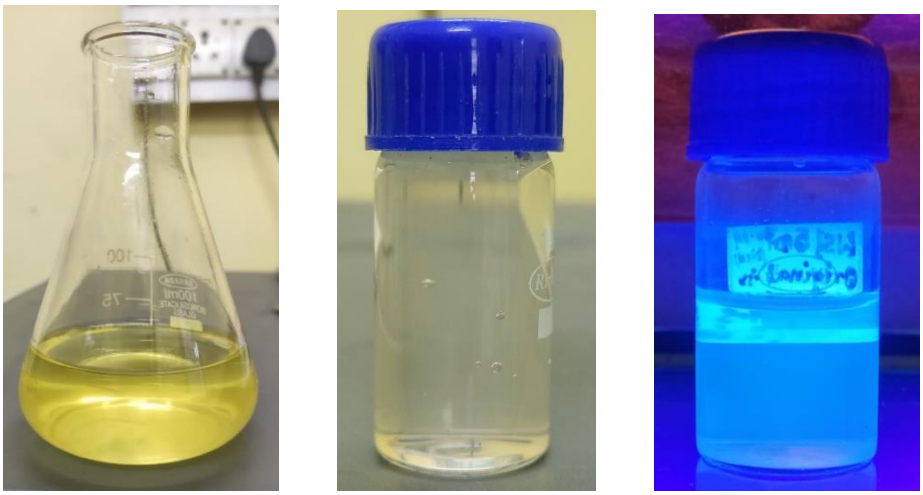

(a) **(b)** **(c)**

Fig: 3.4 (a) Photo image of as-prepared WS_2-QDs solution (b) WS_2 QDs solution after filtration by dialysis bag for 2-3 days. (c) WS_2 QDs under UV light to show the luminescence.

3.4 Sample preparation for Characterization

3.4.1 Si-Wafer cleaning:

In this experiment, we have used a boron (B) doped p-Si wafer (100) of thickness 380 μm (4") purchased from the TED PELLA, INC. as a substrate. The de-ionized (DI) water (ρ = 18 MΩ-cm) obtained from Milli-Q water plant (Millipore, USA). Firstly, we have taken a p-type silicon wafer and cut it into small pieces with the help of diamond cutter. Then wafer was dipped into the TCE (Try-chloro ethylene) in a beaker and was boiled for 5 mins (optimal) and then it was further sonicated for another 5-10 mins. This process removes the dust particle present in the Si wafer as impurity. Secondly the wafer was dipped into Acetone and was sonicated for 5-10 minutes at room temperature. It removes oil and grease from the surface. To remove the inorganic compounds, present in the sample, a **1:1** mixture of $\mathbf{H_2SO_4}$ and $\mathbf{H_2O_2}$ was prepared. For the sake of convenience 5 c.c. of each compound are used (as 1 c.c. is difficult to measure). The wafer was added to the mixture and was left inside the enclosed reaction chamber till the reaction stops. The reaction is exothermic in nature i.e., it produces heat and gas. This reaction completes approximately within 10 mins. Lastly, the sample was dipped into 10% HF solution as Si get converted into its oxide form by making reaction with nearby oxygen particles present in the air. This is an excellent insulator or dielectric material. This is also found as impurity in Si wafer. To remove it the last step in essential. Then the wafers were used for sample preparation by drop casting the solution onto the wafer.

3.4.2 Glass-Slide cleaning:

We have taken a 75 mm long, 25 mm wide glass slide with a thickness of 1.35 mm purchased from Blue Star Micro slides and cover glass. The glass slide was then evenly divided with the help of diamond cutter. Each glass pieces were thoroughly cleaned to remove dust particles from the glass surface. Then each glass pieces were dipped into the TCE (Try-chloro ethylene) in a biker, then it was boiled for 5 mins (optimal) and then it was sonicated for another 5-10mins. This process removes the dust particle present in the glass as impurity. Secondly the glass pieces were dipped into Acetone and was sonicated for 5-10 minutes at room temperature. It removes oil and grease from the surface. To remove the inorganic compounds, present in the sample, a **1:1** mixture of $\mathbf{H_2SO_4}$ and $\mathbf{H_2O_2}$ was prepared. For the sake of convenience 5 c.c. of each compound are used (as 1 c.c. is difficult to measure). The glass pieces were added to the

mixture and was left inside the enclosed reaction chamber till the reaction stops. The reaction is exothermic in nature i.e., it produces heat and gas. This reaction completes approximately within 10 mins. After that the glass pieces were used for sample preparation by drop casting the solution onto the glass.

3.4.3 Characterization Techniques:

A Bruker D8 Advance powder diffractometer was used to characterize the phase structure. Transmission electron microscopy (TEM) and high-resolution transmission electron microscopy (HRTEM) on the samples provided additional microstructural information using a JEOL-3010 transmission electron microscope. The UV–vis spectra were captured using a Jasco V-630 spectrophotometer (USA) and a standard 10-mm quartz cuvette. The photoluminescence (PL) and photoluminescence excitation (PLE) spectra of the as-prepared samples were measured with a Hitachi F-4500 florescence spectrophotometer and an excitation source of a 150 W Xenon lamp. A red-light laser was used to take Raman measurements in ambient conditions. The scattered light was collected using the same objective lens and distributed using a Horiba iHR320 spectrometer.

CHAPTER – 4

Structural, Morphological and Optical Characterization of WSe_2 Nanosheets and WS_2 Quantum Dots on Si Substrates

4.1 Structural and Morphological Characterization of WSe_2 Nanosheets

The as-prepared WSe_2 NSs are analysed by structural and morphological characterization technique such as Transmission Electron Microscopy (TEM), Scanning electron microscopy (SEM) and X-ray diffraction (XRD) at room temperature.

4.1.1 Scanning Electron Microscopy (SEM):

The SEM image of as obtained WSe_2 powder sample from hydrothermal method is shown in Fig 4.1. The obtained WSe_2 has a multilayer nanosheets structure, as can be seen in the image. A graphene-like structure made of extremely thin, curved, few-layer nanosheets with some folded corners is visible in a high-magnification SEM image of the porous WSe_2[67]. The lower magnification image shows two main variations, darker or clearer, which can be correlated to the two orientations of nanosheets to the substrate, parallel or perpendicular respectively[26]. Fig. 4.1 shows the SEM images of WSe_2 NSs at different magnification level.

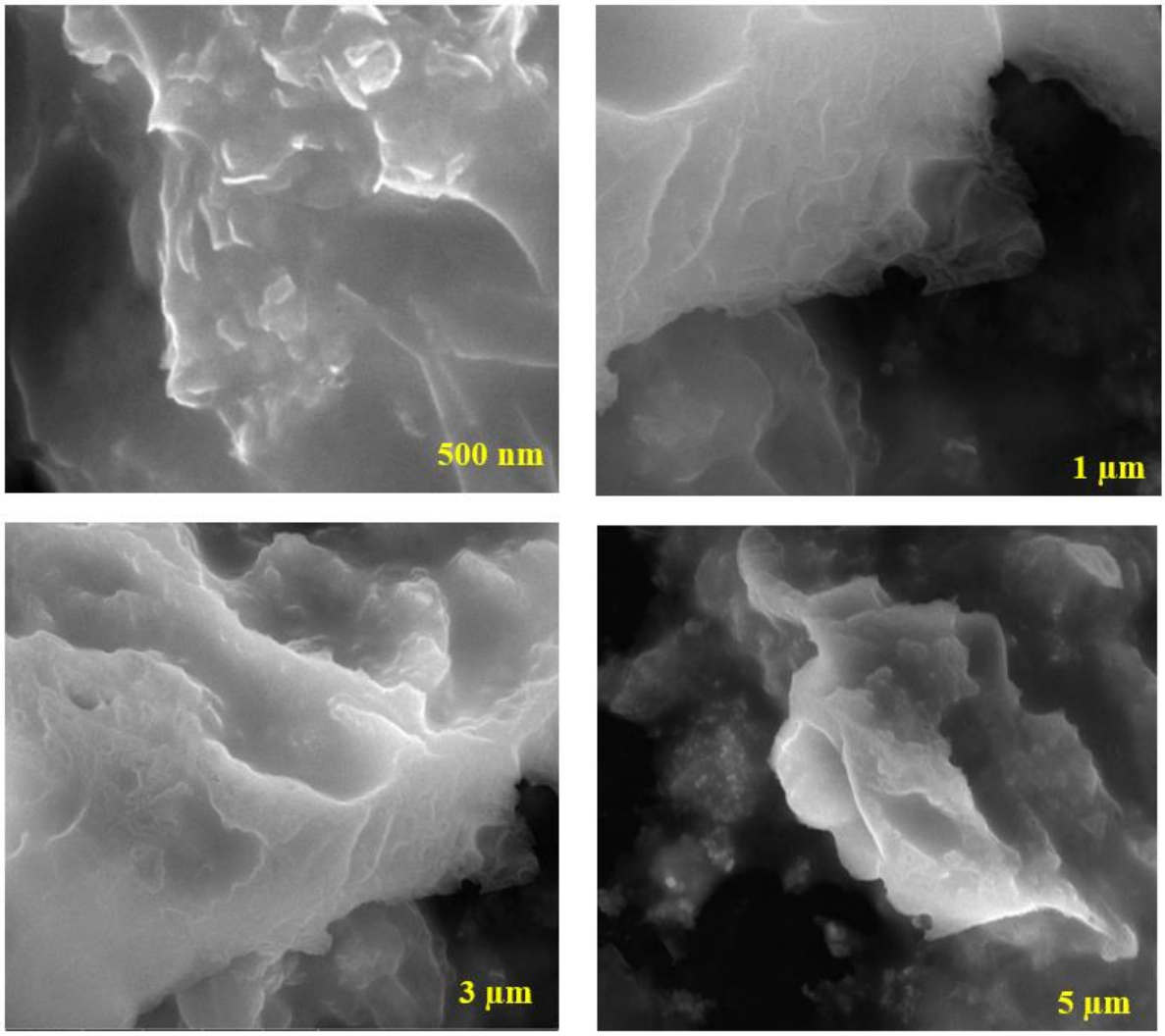

Fig 4.1 SEM images of WSe_2 nanosheet (powder sample)

4.1.2 Transmission Electron Microscopy (TEM):

The TEM images of as synthesised WSe_2 nanosheets at various magnification levels is shown in Fig. 4.2. The dark fringes associated with the (100) planes, which have an interlayer spacing of 0.275 nm, can be seen in a TEM image of a nanosheet with a prominent edge. The nanosheets are curved and folded, as shown by the TEM images. The edges that are visible may offer more active sites for Hydrogen Evolution Reaction (HER) reactions [26]. In order to investigate the composition and number of layers in WSe_2 nanosheets, HRTEM was acquired. From the TEM images, it is clearly visible that number of WSe_2 nanosheets are visible, as shown in Fig. 4.1(b), indicating that they typically have 9 to 15 layers in numbers. The lattice spacing of 0.275 nm in Figure 4.1(b) corresponds to the 2H-(100) WSe_2 plane, which is consistent findings of other researchers in the literature [67].

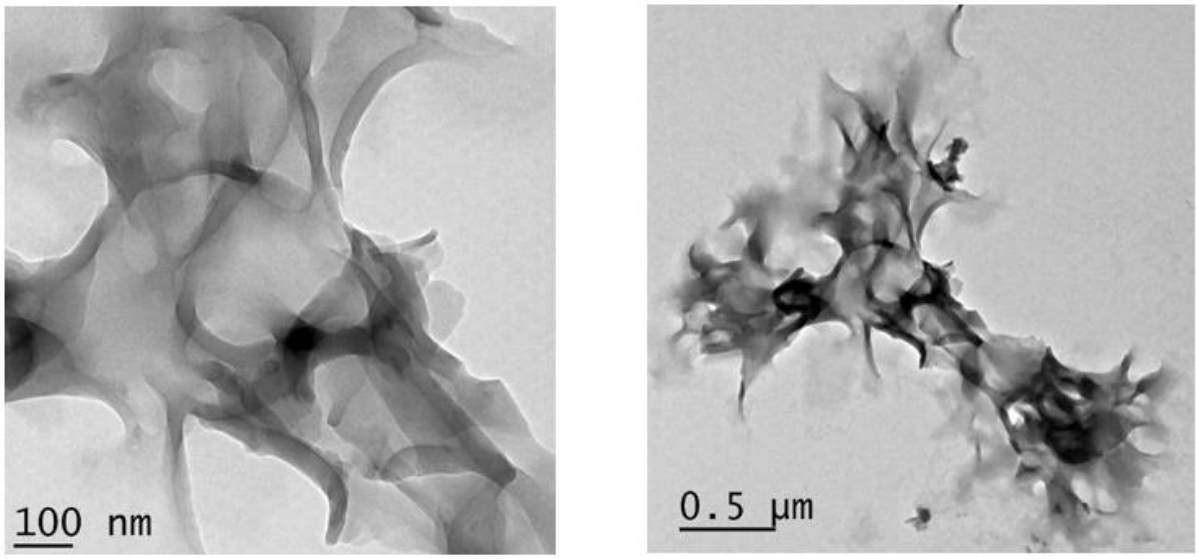

(a)

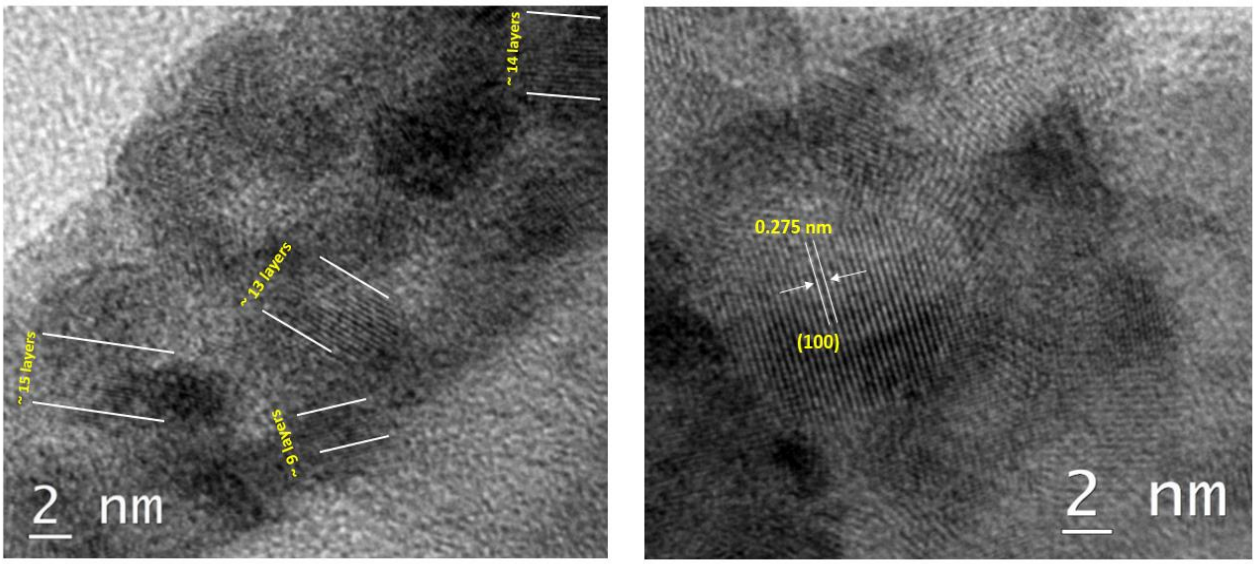

(b)

Fig 4.2 (a) TEM images of WSe_2 Nanosheets (b) HRTEM images of WSe_2 Nanosheet edges

4.1.3 X-ray Diffraction (XRD):

The XRD pattern of as-prepared WSe_2 NSs based powder sample is shown in Fig 4.3. With lattice constants of a = 3.286Å and c = 12.983Å, which matches with the standard values, all significant observed diffraction peaks could be assigned to the hexagonal WSe_2 (JCPDF card No. 38-1388). Additionally, no other distinguishing diffraction peaks are seen, proving that pure WSe_2 was successfully obtained[67]. The XRD pattern of the WSe_2 sample prepared on glass reveals the presence of very intense peaks at 16.69°, 27.55°,32.4°, 43.0°, 48.6° and 51.81° in agreement with the (002), (100), and (103), (105), (110) and (108) diffraction planes of the hexagonal WSe_2 respectively (space group P63/mmc, JCPDS card (no. 38-1388)). The presence of nanosheets with a c-axis parallel to the surface and van der Waals planes perpendicular to the substrate surface and narrow full width at half maximum (FWHM) peak intensities indicates that the sample is crystalline [26, 67, 68], which supports the findings of the SEM[26].

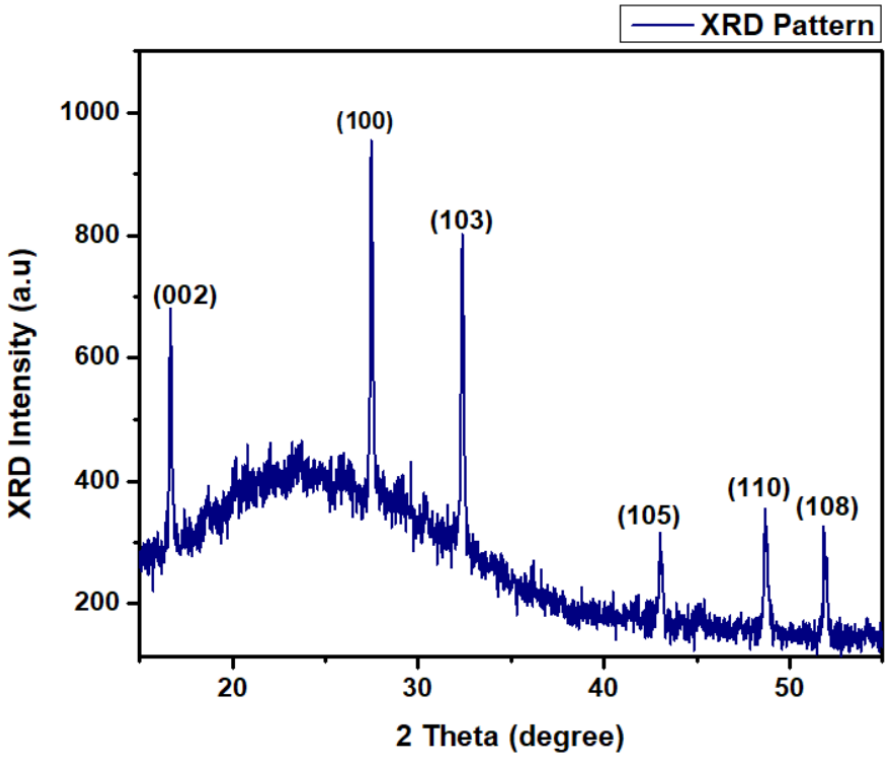

Fig 4.3 The XRD of WSe_2 Nanosheets (powder sample)

4.2 Optical Characterization of WSe_2 Nanosheets

The as-prepared WSe_2 NSs are analysed by optical characterization technique such as excitation wavelength dependent PL spectra, UV-Visible spectrum and Raman spectroscopy at room temperature.

4.2.1 Photoluminescence Spectrum (PL):

The PL spectrum of WSe_2 NSs based on powder dispersed in DI water is shown in Fig. 4.4. All of the PL spectra in this thesis were recorded at room temperature. To excite the WSe_2 NSs solution for PL measurements, we have used a 532 nm solid state laser. As mentioned in Chapter 1, WSe_2 NSs exhibit good luminescence properties due to the transition from indirect to direct bandgap [69]. The observation of good PL demonstrates that the as-synthesized nanostructure of WSe_2 has a direct band gap with a peak intensity at 430 nm when excited with 375 nm laser light. According to Fig. 4.4(a), the PL spectra of a WSe_2 NSs powder-based solution were observed at various excitation wavelengths. It demonstrates how the emission peak shifts and its intensity rises over emission wavelengths as the excitation wavelength is increased from 320 nm to 380 nm. A maximum excitation wavelength of 375 nm and a maximum emission wavelength of 430 nm were observed in the photoluminescence excitation (PLE) spectra of WSe_2 NSs[69].

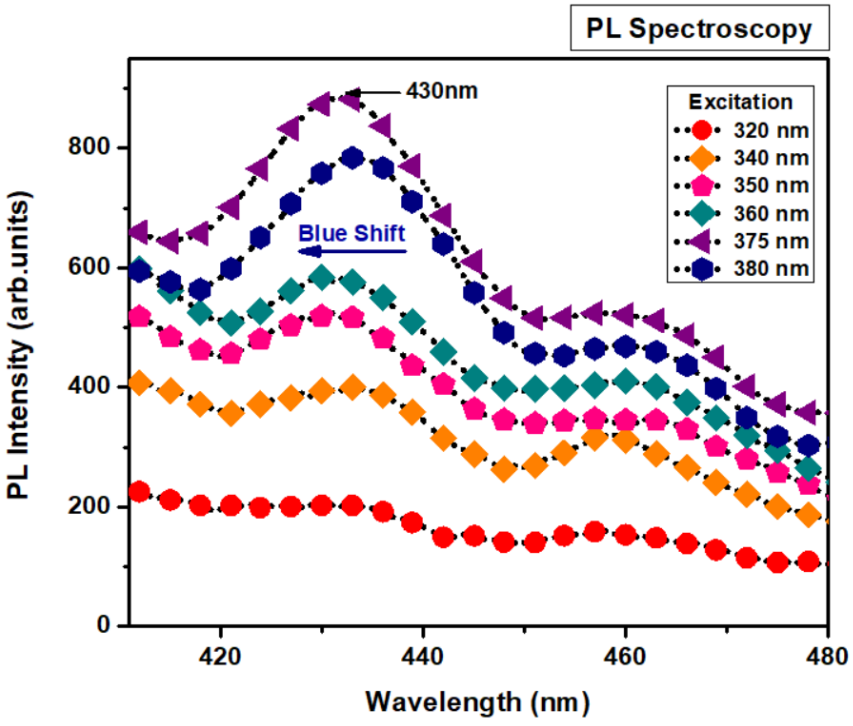

(a)

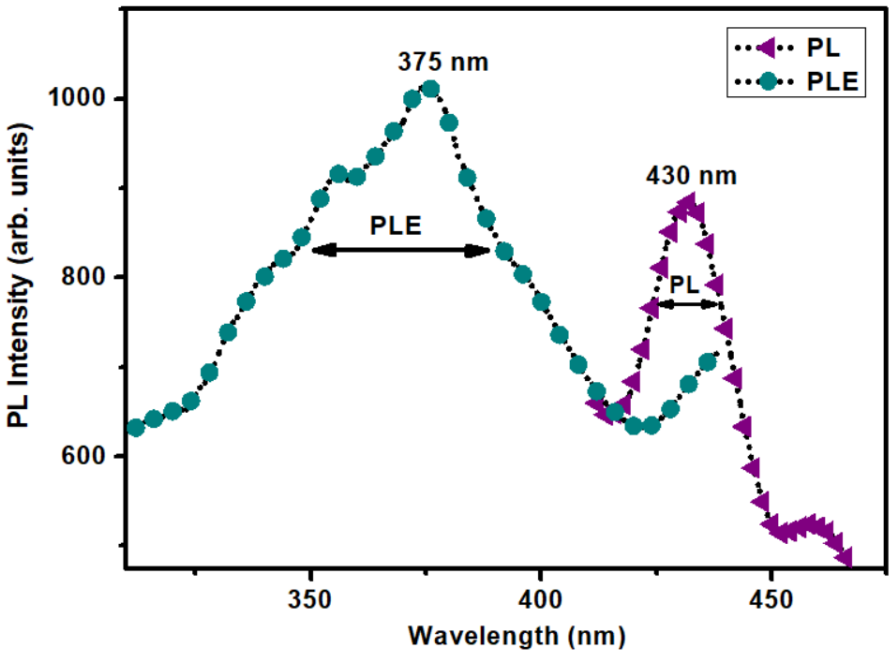

(b)

Fig 4.4 (a) PL-Spectrum of WSe_2 Nanosheets for different excitation. (b) Excitation and emission PL spectra of WSe_2 Nanosheets

4.2.2 UV – Vis Spectrum:

The UV-Vis technique is required for the optical study of materials. Optical research aids researchers in the development of nanomaterial applications for a variety of applications. The optical properties of materials, particularly solar cells, are used to fabricate various devices. This technique can be used to calculate the optical band gap, which aids in the selection of materials for energy conversion purposes such as converting light energy to electrical energy in a solar cell. The purity of the sample can also be measured using this technique by comparing it to the reference solution. The results of various materials are described here, which can aid in understanding the analysis of UV- vis spectroscopy results. The UV-vis spectrum of as-prepared WSe_2 NSs based on powder dispersed in DI water is shown in Fig. 4.5 At wavelengths of 408.29 nm and 751.73 nm, respectively, are where the excitonic absorption peaks of A and B are found. These are visible as a result of the direct transition gap at point K. According to the PL results, the appearance of an excitonic transition, which is red-shifted from the single layer transition, shows that the synthesized nanosheets have fewer layers[12]. The WSe_2 spectrum displays additional A' and B' absorption peaks as a result of the superpositions of the Se p- and W d-orbitals as well as adjacent layers[26]. As a result of the superpositions of the

Se p-orbitals with W d-orbitals, as well as adjacent layers, the WSe_2 spectrum shows other absorption peaks of A' and B'. Because the d-electron band is disturbed at the level of intra-layer and inter layer by the Se p-orbitals, the excitonic existence of these peaks may result from the splitting of the ground and excited states of the two transitions of A and B[12, 70].

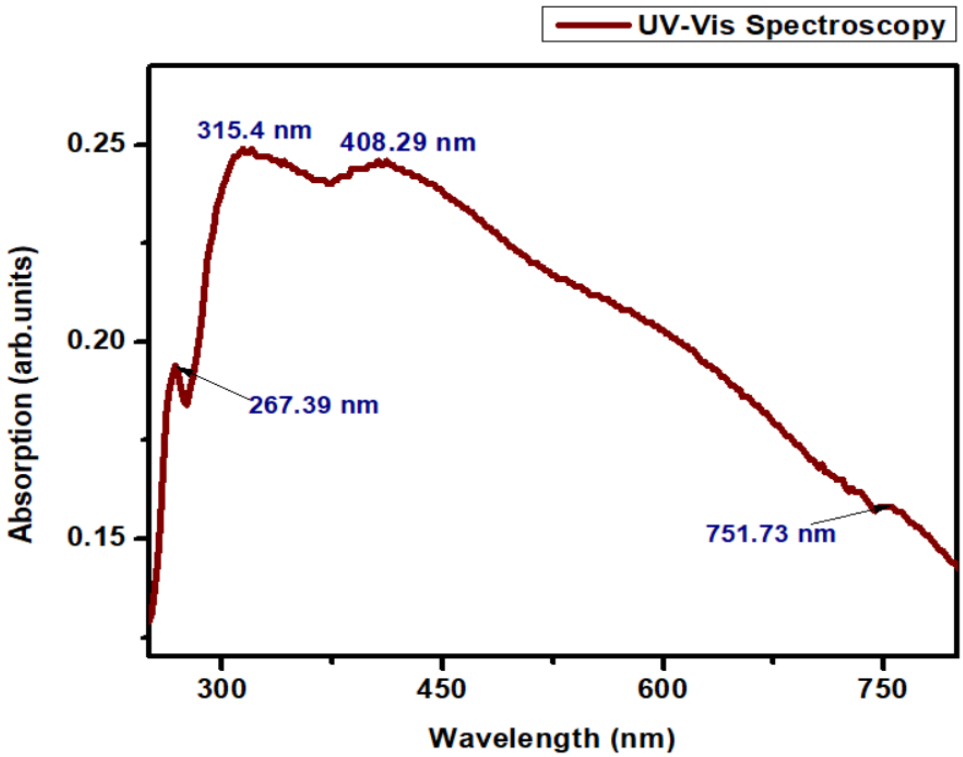

Fig: 4.5 The absorption spectra of WSe_2 Nanosheets

4.2.3 Raman Spectroscopy:

The Raman spectrum of as-prepared WSe_2 NSs based thin film coated on glass substrates is shown in Fig. 4.6. Additionally, it is a crucial tool for revealing the optical characteristics of TMDC materials and the total number of layers in the samples [71]. Two unresolved peaks at 250 cm^{-1} and 303 cm^{-1} are clearly visible on a Raman spectrum of WSe_2 that was captured using an argon laser which is excited at a 532 nm wavelength[71]. The E^1_{2g} mode is consistent with the observed peak at 250 cm^{-1} (in-plane vibrational mode). The A_{1g} mode is the shoulder peak seen at 303 cm^{-1}, which is connected to the out-of-plane mode. This indicates that there is a significant bond vibration between W and Se along the vertical layer direction [26].

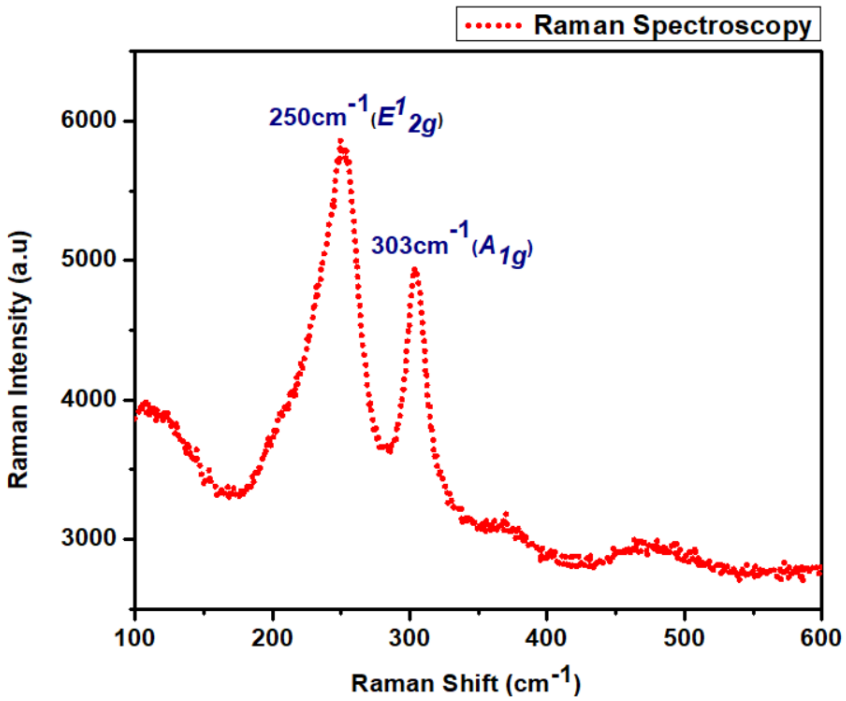

Fig 4.6 The Raman spectra of WSe_2 Nanosheets prepared using hydrothermal method

4.3 Structural and Morphological Characterization of WS_2 Quantum Dots

The as-prepared WSe_2 QDs are analysed by structural and morphological characterization technique such as atomic force microscopy (AFM) and X-ray diffraction (XRD) at room temperature.

4.3.1 Atomic Force Microscopy (AFM):

The AFM images of WS_2 QDs based thin film coated on Si substrates is shown in Fig. 4.7. We can clearly see the highly dispersed QDs over the substrate from here. The height profile of quantum dots shows an average height of ~6 nm, which corresponds to multilayer WS_2-QDs [72, 73]. Generally, the heights of the QDs were mostly 2.5–4.0 nm, corresponding to three to five single layers of WS_2.

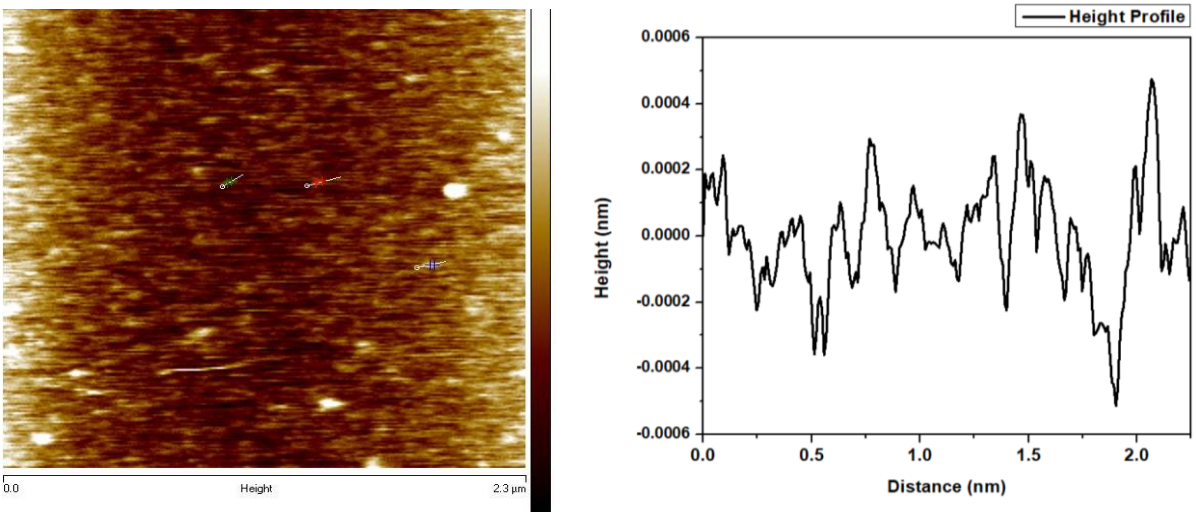

(a) (b)

Fig 4.7 (a) AFM image of WS_2 QDs based thin film coated on Si substrates. (b) Height profile of WS_2 QDs

4.3.2 X-ray Diffraction (XRD):

The XRD pattern of WS_2 QDs based thin film coated on p-Si substrates is shown in Fig. 4.8. In general, the XRD pattern of the bulk WS_2 powder shows maximum diffraction peaks. In accordance with other reports, all of the bulk WS_2 powder's recorded diffraction peaks can be assigned to the WS_2 phase[74, 75]. The bulk material exhibits periodicity in the c-axis, with an effective peak (002) found at $\theta = 14.3°$. However, the previous research has shown that when TMDCs, like WS_2, are converted to their single layer and QDs forms, the (002) peak vanishes. For the majority of samples, Ren *et al.* [74] have demonstrated that there is no noticeable peak seen in XRD patterns when the size of the particle is very small. The formation of QDs, according to Wu *et. al.* research's [76], prevents the XRD pattern for WS_2/MoS_2 from showing any sign of a signal or peak. The absence of a peak associated with WS_2 QDs in the XRD pattern, as shown in the figure, clearly establishes the presence of WS_2 quantum dots in a small size. The disappearance of the distinctive peaks indicates that the structure of the as-prepared WS_2 QDs is very small and thin[77]. This is also supported by works reported by Singh *et al.* [73] for WS_2 QDs based graphene nanocomposite film for UV detections.

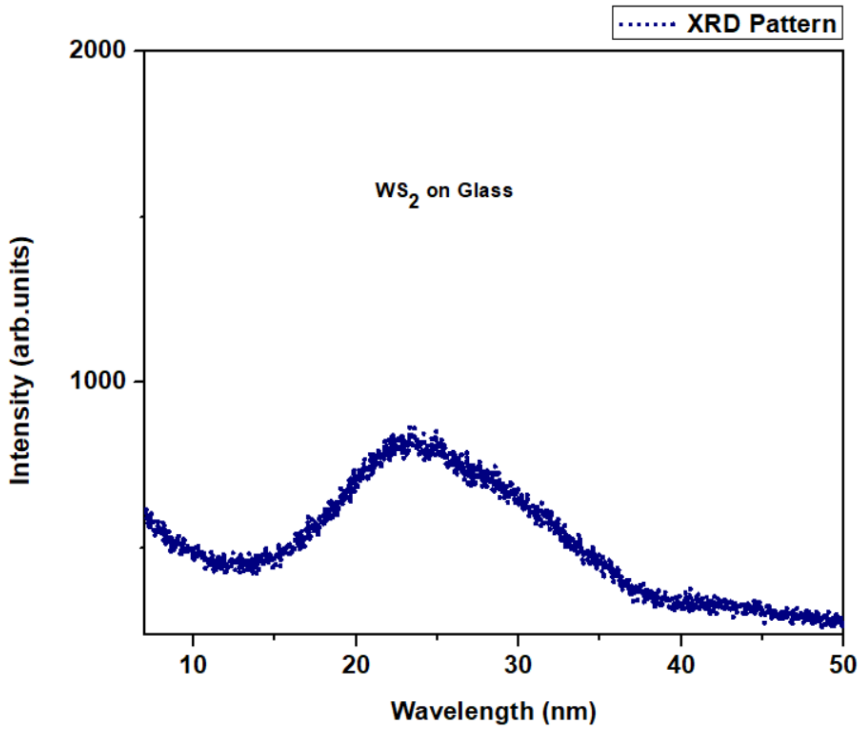

Fig 4.8 The XRD pattern of WS_2 Quantum Dots based thin film coated on Si substrates

4.4 Optical Characterization of WS_2 Quantum Dots

The as-prepared WS_2 QDs are analysed by optical characterization technique such as excitation wavelength dependent PL spectra, UV-Visible spectrum and Raman spectroscopy at room temperature.

4.4.1 UV – Vis Spectrum:

The UV-visible spectrum of as-prepared WS_2 QDs based solution is shown in Fig. 4.9. In general, the four distinctive peaks at 630 nm, 528 nm, 456 nm and 417 nm are generally visible in the raw WS_2 spectrum. The bulk WS_2 absorption spectrum's general characteristics are in strong agreement with other reports[12, 78]. Peaks near 417 nm and 456 nm are attributed to optical transitions from the valence band to the conduction band, whereas peaks near 630 nm and 528 nm are attributed to excitonic absorption caused by direct gap transitions at the K point. The absorption spectra change significantly when microcrystals transform into QDs. The excitonic peaks disappear, and the band edge moves to a shorter wavelength [76]. Due to relatively small size of the WS_2 QDs, a peak at around 308 nm and 374 nm is observed. The band gap caused by quantum confinement effects (QCE) is well known to be size dependent;

that is, the smaller the size, the larger the energy gap. As a result, the enhanced band gap opening is caused by the strong quantum confinement effect[77, 79, 80]. The direct band-gap energy is determined to be 4.07 eV by plotting the square root of the absorption energy (αhγ, where α is the absorbance and hγ is the photon energy) against hγ (known as the Tauc plot), which is much larger than that of the bulk WS_2 (0.97 eV) and monolayer WS_2 (1.79 eV).

In order to find the value of bandgap, by using the following relation

$$\alpha h\gamma = A(h\gamma - E_g)^m \quad (4.1)$$

Where α is absorption coefficient, $\boldsymbol{h\gamma}$is the photon energy, (value of $h = 6.634 \times 10^{-34} j - sec$), m = ½ (for direct allowed transitions)

$$h\gamma = h.\left(\frac{c}{\lambda}\right) \quad (4.2)$$

Where c = velocity of light and λ = wavelength. By plotting the graph between square of absorption energy $(\alpha h\gamma)^2$vs. $h\gamma$ the band gap of as-prepared of WS_2-QDs can be calculated as 4.07 eV. It is well known that the bandgap of a semiconductor increases as the size of the nanostructure approaches the excitonic Bohr radius, which is approximately 1.7 nm[81] for WS_2, it is reasonable to consider the QCE for nanostructures smaller than tens of nanometres.

In order to calculate the Bohr radius of WS_2 by using the following equation

$$R_B = \epsilon r_h \left(\frac{1}{m_e^*} + \frac{1}{m_h^*}\right)$$

where ε = relative dielectric constant and r_h = Bohr radius of the hydrogen atom. m_e^* and m_h^* = effective masses of the WS_2's electron and hole respectively. ε, r_h, and m_e^* and m_h^* = 4.4, 0.0529 nm, and 0.30 and 0.26, respectively. Thus, R_B calculated as 1.7 nm.

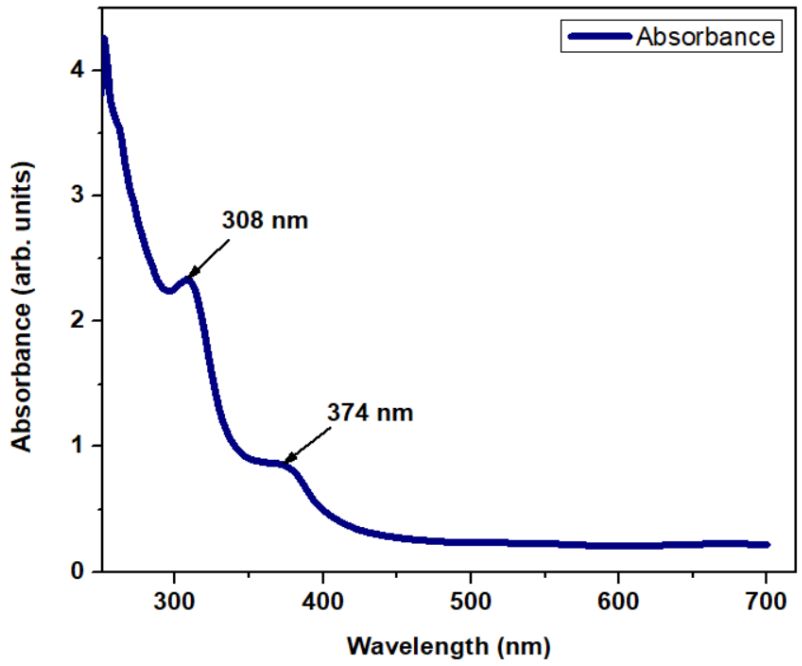

(a)

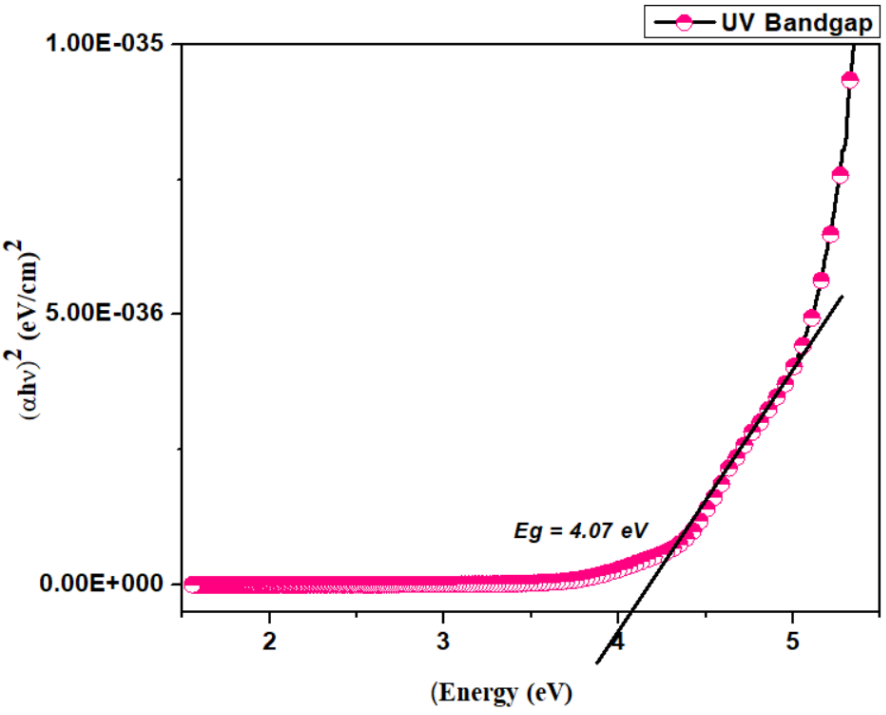

(b)

Fig: 4.9 (a) Absorption spectra (b) Energy-Band gap calculations of WS_2 QDs

4.4.2 Photoluminescence Spectrum (PL):

The photoluminescence spectrum of as-prepared WS_2 QDs based solution is shown in Fig. 4.10. The photoluminescence properties of the prepared WS_2 QDs dispersion were studied at various excitation wavelengths ranging from 380 to 440 nm. Excitation-dependent PL is observed, and the PL peak position corresponds well to the size distribution. The maximum emission is observed to be around 490 nm, with an excitation wavelength of 410 nm. The intensity of photoluminescence increases until the excitation wavelength reaches 410 nm almost for maximum excitation wavelength and then decreases, which is consistent with other methods of producing WS_2 QDs [74, 77]. The prepared WS_2 quantum dots exhibit polydispersity, a property of our synthesis method, as evidenced by their excitation-dependent photoluminescence. On the other hand, WS_2 QDs exhibit enhanced photoluminescence in the blue spectral region at room temperature and have a significantly higher direct transition energy than the bulk. Further the detection wavelength was set at the characteristic emission position for PL excitation (PLE). Fig 4.10 (b) depicts the PLE spectrum at 405 nm detection wavelength. We discovered a clear PLE peak at 490 nm.

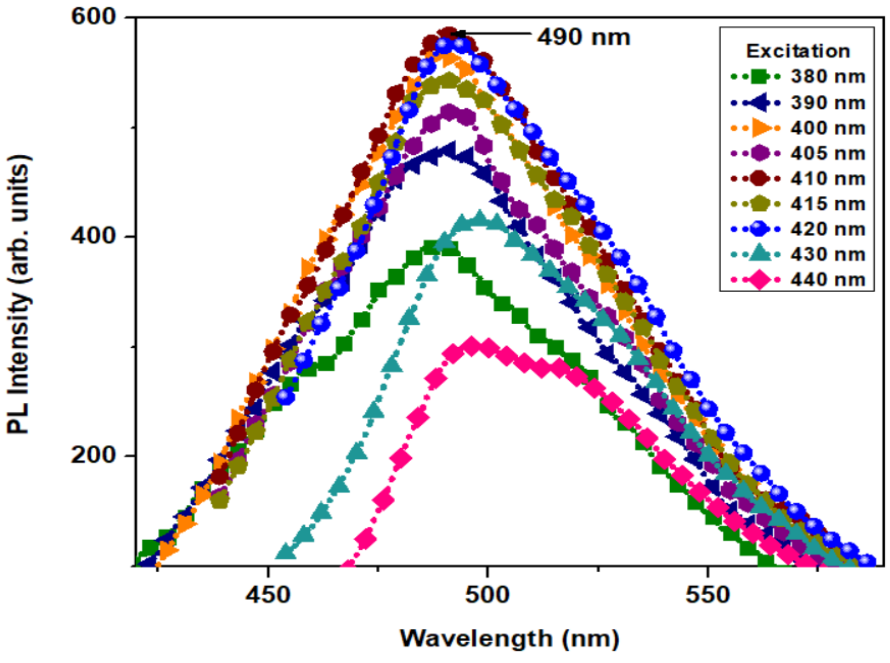

(a)

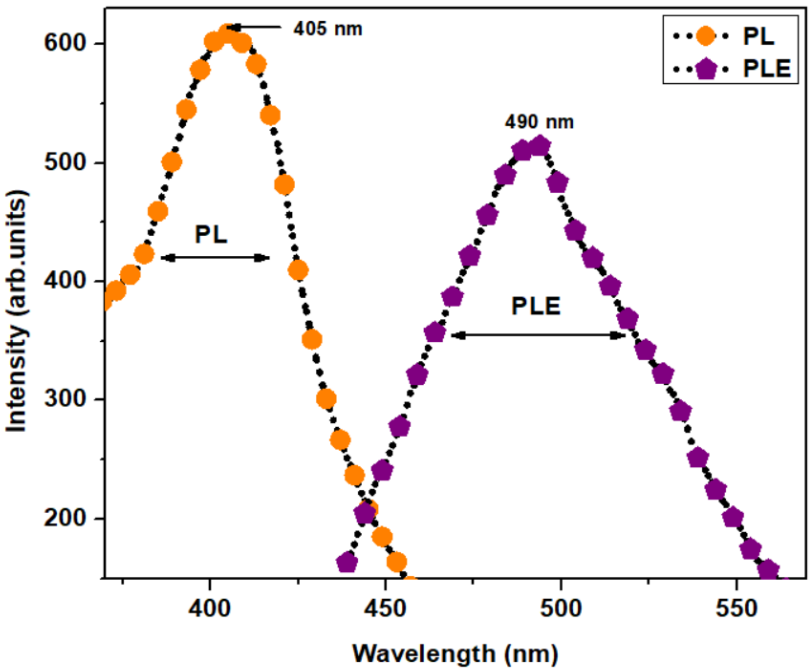

(b)

Fig 4.10 (a) PL-Spectrum of WS_2 QDs for different excitation. (b) Excitation and emission PL spectra of WS_2 QDs

4.4.3 Raman Spectroscopy:

Raman spectroscopy has been widely used to obtain additional complementary information from ultrathin 2D-layered nanomaterials [82]. The as-grown WS_2-QDs were characterized by a nondestructive Raman spectroscopy technique. Raman spectra were collected using a Raman spectrophotometer with a 532 nm laser excitation. The Raman spectrum of bulk WS_2 (WS_2 powder) consists of many first-order and second-order peaks, out of which, there are four Raman-active modes for 2D-layered TMD compounds: A_{1g}, E_{1g}, E^1_{2g}, and E^2_{2g} modes. Because of the forbidden selection rule in the typical back-scattering measurement geometry and and limited rejection against Rayleigh scattering, respectively E_{1g} mode and E^2_{2g} mode is rarely found in reports[82, 83]. Generally, WS_2 powder showed two peaks at 415 cm^{-1} and 348 cm^{-1}, corresponding to the first order in-plane E^1_{2g} and the out-of-plane A_{1g} phonon modes of 2H-WS_2, respectively. The key feature of these modes is that the frequency difference between them can reveal the number of layers in the nanosheets. These two peaks were generally absent in QDs due to the decreased interlayer van der Waals force [76, 83]. The Raman spectrum of as-prepared WS_2 QDs based thin film coated on glass substrates is shown in Fig. 4.11 In this

case, only single WS_2 peak was observed at 396 cm^{-1} corresponding to the in-plane (E^1_{2g}). Only one peak at 396 cm^{-1} is visible that reveals the signature of WS_2.

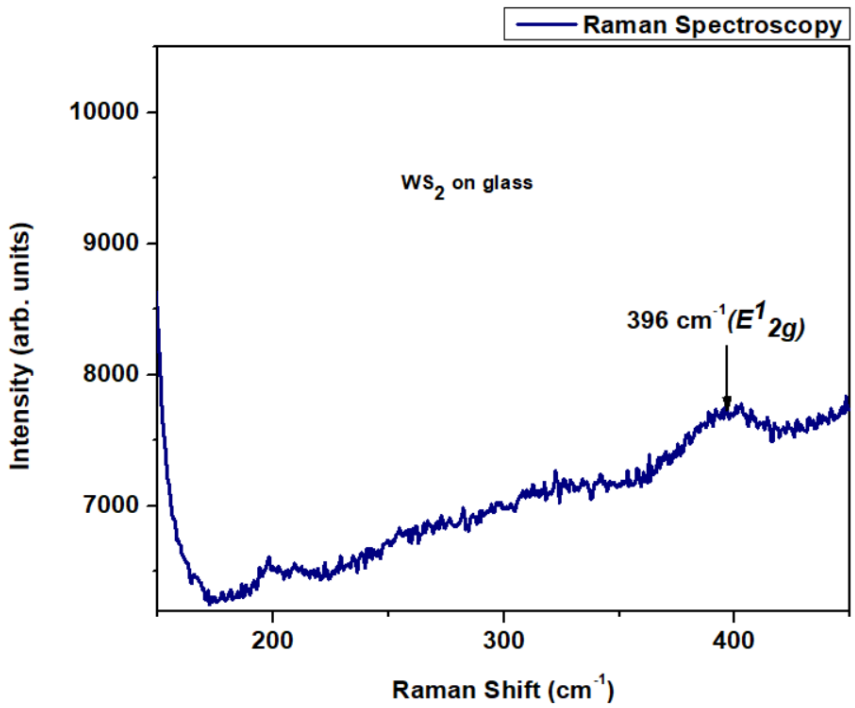

Fig 4.11 The Raman spectra of WS_2 Quantum Dots

CHAPTER – 5

Conclusion and Future Scope

5.1 Introduction

The basic objective of thesis is to present a detailed analysis of the synthesis process of various nanostructures of TMDCs materials and detailed analysis of the different structural, morphological and optical characteristics of as prepared WSe_2 Nanosheets and WS_2 Quantum Dots. The purpose of this chapter is to summarize and conclude the major observations presented in the previous chapters of this thesis. We also attempted to outline some future work related to the areas covered in this thesis.

Chapter-1, discusses some basic fundamentals of TMDCs as a 2D material, specifically the crystal structure and band structure of one of the most important 2D-TMDC materials, i.e., WS_2 and WSe_2. We used DFT calculations to analyse the band structure of WS_2 and WSe_2 with varying number of layers using Quantum–ATK Software. A direct band gap of 1.55 eV and 1.79 eV is observed for monolayer WSe_2 and WS_2, whereas an indirect band gap is observed for bulk WSe_2 and WS_2, demonstrating the suitability of monolayer WSe_2 and WS_2 for optoelectronics applications. Further, some phenomenon related to nanostructure of 2D Materials such as quantum confinement, particle in a box discussed in the details.

Chapter-2, includes a review of some important state-of-the-art works on the synthesis and characterization of some 2D based TMDC materials. A comprehensive review of the literature on the reported structural and optical characteristics of WSe_2 Nanosheets and WS_2 quantum Dots is presented.

Chapter 3, includes the complete experimental details of WSe_2 Nanosheets and WS_2 Quantum Dots. WSe_2 NSs and WS_2 QDs were synthesised by simple facile colloidal method. The synthesis process followed here is hydrothermal synthesis by using chemicals like sodium tungstate dihydrate and L-cysteine as W and S source. WSe_2 nanosheets are synthesized with

N, N-dimethylformamide as the solvent for selenium powder, which cooperates with a reducing agent, that is, sodium borohydride and sodium tungstate dihydrate.

Chapter 4, discusses the characterization result of WSe_2 Nanosheets and WS_2 Quantum Dots. The experimental results showed that the resulting NSs as well as QDs had a good PL (at 375 nm and 410 nm excitation respectively) characteristics. The TEM spectra were used to characterize the surface of WSe_2 NSs to calculate the no of layers present in the as obtained nanosheets. AFM were used to characterize the particle size and height profile of the as prepared WS_2 QDs. XRD were used to characterize the crystallinity of as prepared QDs and NSs. Further UV Visible spectra, excitation dependent PL spectra, and Raman spectra were used to characterize as-synthesised NSs and QDs. The PL spectrum of WSe_2 shows a sharp peak at 430 nm at an excitation wavelength of 375 nm and for WS_2 QDs a sharp peak at 490 nm at an excitation wavelength of 410 nm which matches previous reports in the literature. The bandgap of WSe_2 NSs and WS_2 QDs based solution sample has been determined by UV-vis spectrum. The Raman spectra shows two peaks for WSe_2 NSs. The observed peak at 250 cm^{-1} corresponds to the $E_{2g}{}^1$ mode which is in-plane vibrational mode. The shoulder peak observed at 303 cm^{-1}, associated with the out-of-plane mode, is the A_{1g} mode. This means that there is a significant vibration along the vertical layer direction. Due to the reduced interlayer van der Waals force, the Raman spectra of WS_2 QDs do not exhibit any obvious peaks.

5.2 Future Scope

Semiconducting TMDCs materials have been used in many application areas such as photo detector, solar cell, light emitting diodes, sensors, photo transistors etc. In this thesis we have worked on the complete synthesis and characterization process of WSe_2 NSs on n-Si substrates and WS_2 QDs on p-Si substrate. So, for the future work we can fabricate the following device structures based on WS_2 QDs and WSe_2 NSs. We will fabricate the photodetector based on hybrid structure (0D-2D) of semiconducting n-WS_2 quantum dots (0D) with p-WSe_2 NSs (2D) on n-Si/ITO substrates. According to our findings, the hybrid structure of WS_2-QDs with WSe_2 Nanosheets can be a promising candidate for high-performance optoelectronic devices. The schematic diagram of the proposed device structure is shown in Fig. 5.1 and Fig. 5.2.

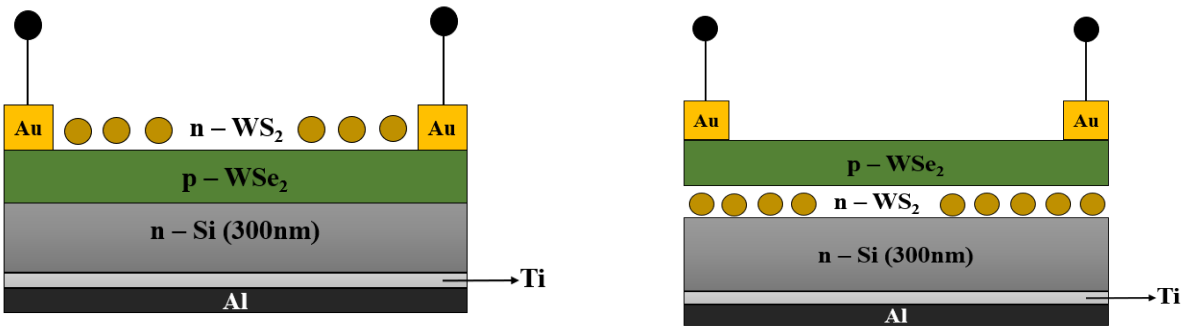

Fig. 5.1 Schematic Device Structure of Al/Ti/n-Si/p-WSe_2/n-WS_2/Au and Al/Ti/n-Si/n-WS_2/p-WSe_2/Au

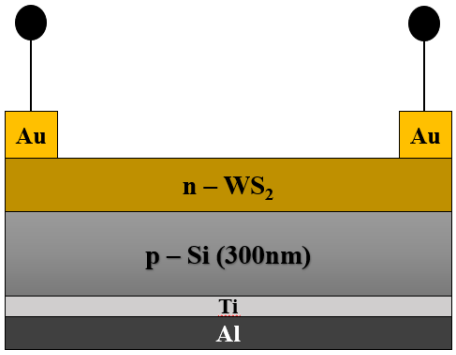

Fig. 5.2 Schematic Device Structure of Al/Ti/p-Si/WS_2/Au

5.3 References

1. Bhuyan, M.S.A., et al., *Synthesis of graphene.* International Nano Letters, 2016. **6**(2): p. 65-83.
2. Yadav, C. and Y. Chauhan, *Modeling of Transition Metal Dichalcogenide Transistors for SPICE Simulation at MOS-AK Workshop, Berkeley, Dec. 2016*. 2016.
3. Bernardi, M., et al., *Optical and Electronic Properties of Two-Dimensional Layered Materials.* Nanophotonics, 2017. **6**(2): p. 479-493.
4. Wang, J.L. *Strain Engineering of Two-Dimensional (2D) Materials at the Atomic Scales*. 2018.
5. Ahmed, S. and J. Yi, *Two-Dimensional Transition Metal Dichalcogenides and Their Charge Carrier Mobilities in Field-Effect Transistors.* Nano-micro letters, 2017. **9**(4): p. 50-50.
6. Kolobov, A.V. and J. Tominaga, *Two-Dimensional Transition-Metal Dichalcogenides*. Vol. 239. 2016.
7. Chowdhury, S., P. Venkateswaran, and D. Somvanshi. *A comparative study of biaxial strain modulated electronic structure of MSe2 (M = W, Mo) monolayer*. in *2021 5th International Conference on Electronics, Materials Engineering & Nano-Technology (IEMENTech)*. 2021.
8. Wang, Q.H., et al., *Electronics and optoelectronics of two-dimensional transition metal dichalcogenides.* Nat Nanotechnol, 2012. **7**(11): p. 699-712.
9. Jo, S., et al., *Mono- and Bilayer WS2 Light-Emitting Transistors.* Nano Letters, 2014. **14**(4): p. 2019-2025.
10. Mahler, B., et al., *Colloidal Synthesis of 1T-WS2 and 2H-WS2 Nanosheets: Applications for Photocatalytic Hydrogen Evolution.* Journal of the American Chemical Society, 2014. **136**(40): p. 14121-14127.
11. Wilson, J.A. and A.D. Yoffe, *The transition metal dichalcogenides discussion and interpretation of the observed optical, electrical and structural properties.* Advances in Physics, 1969. **18**: p. 193-335.
12. Zhao, W., et al., *Evolution of Electronic Structure in Atomically Thin Sheets of WS2 and WSe2.* ACS Nano, 2013. **7**(1): p. 791-797.
13. Roy, S. and P. Bermel, *Electronic and optical properties of ultra-thin 2D tungsten disulfide for photovoltaic applications.* Solar Energy Materials and Solar Cells, 2018. **174**: p. 370-379.
14. Mak, K.F., et al., *Atomically Thin ${\mathrm{MoS}}_{2}$: A New Direct-Gap Semiconductor.* Physical Review Letters, 2010. **105**(13): p. 136805.
15. Gusakova, J., et al., *Electronic Properties of Bulk and Monolayer TMDs: Theoretical Study Within DFT Framework (GVJ-2e Method).* physica status solidi (a), 2017. **214**(12): p. 1700218.
16. Mu, C., J. Xiang, and Z. Liu, *Photodetectors based on sensitized two-dimensional transition metal dichalcogenides—A review.* Journal of Materials Research, 2017. **32**(22): p. 4115-4131.
17. Radisavljevic, B., et al., *Single-layer MoS2 transistors.* Nature Nanotechnology, 2011. **6**: p. 147.
18. Nengjie, H., Y. Yujue, and L. Jingbo, *Optoelectronics based on 2D TMDs and heterostructures.* Journal of Semiconductors, 2017. **38**(3): p. 031002.
19. Huang, C., et al., *Lateral heterojunctions within monolayer MoSe2–WSe2 semiconductors.* Nature Materials, 2014. **13**: p. 1096.
20. Zhang, K., et al., *Interlayer Transition and Infrared Photodetection in Atomically Thin Type-II MoTe2/MoS2 van der Waals Heterostructures.* ACS Nano, 2016. **10**(3): p. 3852-3858.
21. Chowdhury, S., P. Venkateswaran, and D. Somvanshi, *A systematic study on the electronic structure of 3d, 4d, and 5d transition metal-doped WSe2 monolayer.* Superlattices and Microstructures, 2020. **148**: p. 106746.
22. Cheiwchanchamnangij, T. and W.R.L. Lambrecht, *Quasiparticle band structure calculation of monolayer, bilayer, and bulk MoS${}_{2}$.* Physical Review B, 2012. **85**(20): p. 205302.

23. Deng, S., L. Li, and M. Li, *Stability of direct band gap under mechanical strains for monolayer MoS2, MoSe2, WS2 and WSe2.* Physica E: Low-dimensional Systems and Nanostructures, 2018. **101**: p. 44-49.
24. Kuc, A., N. Zibouche, and T. Heine, *Influence of quantum confinement on the electronic structure of the transition metal sulfide TS${}_{2}$.* Physical Review B, 2011. **83**(24): p. 245213.
25. Chowdhury, S., P. Venkateswaran, and D. Somvanshi, *Strain-dependent doping behavior of WSe₂ monolayer: A first-principle calculation.* Europhysics Letters, 2022. **137**(2): p. 26004.
26. Sierra-Castillo, A., et al., *Synthesis and Characterization of Highly Crystalline Vertically Aligned WSe2 Nanosheets.* Applied Sciences, 2020. **10**(3).
27. Gopal, R., et al., *Quantum Confinement Effect of 2D Nanomaterials*. 2020.
28. Luo, G., et al., *Quantum dot behavior in transition metal dichalcogenides nanostructures.* Frontiers of Physics, 2017. **12**(4): p. 128502.
29. *Nanocrystals in their prime.* Nat Nanotechnol, 2014. **9**(5): p. 325.
30. Murray, C.B., C.R. Kagan, and M.G. Bawendi, *Self-Organization of CdSe Nanocrystallites into Three-Dimensional Quantum Dot Superlattices.* Science, 1995. **270**(5240): p. 1335-1338.
31. Dabbousi, B.O., et al., *Electroluminescence from CdSe quantum-dot/polymer composites.* Applied Physics Letters, 1995. **66**(11): p. 1316-1318.
32. Novoselov, K.S., et al., *Two-dimensional gas of massless Dirac fermions in graphene.* Nature, 2005. **438**(7065): p. 197-200.
33. Novoselov, K.S., et al., *Electric field effect in atomically thin carbon films.* Science, 2004. **306**(5696): p. 666-9.
34. Miremadi, B.K. and S.R. Morrison, *High activity catalyst from exfoliated MoS2.* Journal of Catalysis, 1987. **103**(2): p. 334-345.
35. M, T. and D.J. Late, *Temperature dependent phonon shifts in single-layer WS(2).* ACS Appl Mater Interfaces, 2014. **6**(2): p. 1158-63.
36. Novoselov, K.S., et al., *Two-dimensional atomic crystals.* Proc Natl Acad Sci U S A, 2005. **102**(30): p. 10451-3.
37. Coleman, J.N., et al., *Two-dimensional nanosheets produced by liquid exfoliation of layered materials.* Science, 2011. **331**(6017): p. 568-71.
38. Brodie, B.C., *XIII. On the atomic weight of graphite.* Philosophical Transactions of the Royal Society of London, 1859. **149**: p. 249-259.
39. Hummers, W.S. and R.E. Offeman, *Preparation of Graphitic Oxide.* Journal of the American Chemical Society, 1958. **80**(6): p. 1339-1339.
40. Xiong, F., et al., *Li Intercalation in MoS2: In Situ Observation of Its Dynamics and Tuning Optical and Electrical Properties.* Nano Lett, 2015. **15**(10): p. 6777-84.
41. Nicolosi, V., et al., *Liquid Exfoliation of Layered Materials.* Science, 2013. **340**(6139): p. 1226419.
42. Zhan, Y., et al., *Large-area vapor-phase growth and characterization of MoS(2) atomic layers on a SiO(2) substrate.* Small, 2012. **8**(7): p. 966-71.
43. Lee, Y.H., et al., *Synthesis of large-area MoS2 atomic layers with chemical vapor deposition.* Adv Mater, 2012. **24**(17): p. 2320-5.
44. Liu, K.K., et al., *Growth of large-area and highly crystalline MoS2 thin layers on insulating substrates.* Nano Lett, 2012. **12**(3): p. 1538-44.
45. Peters, E.S., C.J. Carmalt, and I.P. Parkin, *Dual-source chemical vapour deposition of titanium sulfide thin films from tetrakisdimethylamidotitanium and sulfur precursors.* Journal of Materials Chemistry, 2004. **14**(23): p. 3474-3477.
46. Boscher, N.D., et al., *Atmospheric pressure chemical vapour deposition of vanadium diselenide thin films.* Applied Surface Science, 2007. **253**(14): p. 6041-6046.
47. Boscher, N.D., C.J. Carmalt, and I.P. Parkin, *Atmospheric pressure chemical vapor deposition of WSe2 thin films on glass—highly hydrophobic sticky surfaces.* Journal of Materials Chemistry, 2006. **16**(1): p. 122-127.
48. Carmalt, C.J., I.P. Parkin, and E.S. Peters, *Atmospheric pressure chemical vapour deposition of WS2 thin films on glass.* Polyhedron, 2003. **22**(11): p. 1499-1505.

49. Boscher, N.D., et al., *Atmospheric Pressure CVD of Molybdenum Diselenide Films on Glass.* Chemical Vapor Deposition, 2006. **12**(11): p. 692-698.
50. Peng, Y., et al., *Hydrothermal Synthesis and Characterization of Single-Molecular-Layer MoS2 and MoSe2.* Chemistry Letters, 2001. **30**(8): p. 772-773.
51. Jeong, S., et al., *Well-defined colloidal 2-D layered transition-metal chalcogenide nanocrystals via generalized synthetic protocols.* J Am Chem Soc, 2012. **134**(44): p. 18233-6.
52. Rukari, T. and A. Babita, *Review Article TRANSMISSION ELECTRON MICROSCOPY-AN OVERVIEW*. 2013. **1**: p. 1-7.
53. Mohammed, A. and A. Abdullah, *Scanning Electron Microscopy (SEM): A Review*. 2019.
54. Wang, Y.-a., et al., *Effects of tumor metabolic microenvironment on regulatory T cells.* Molecular Cancer, 2018. **17**(1): p. 168.
55. Dufrêne, Y.F. and A.E. Pelling, *Force nanoscopy of cell mechanics and cell adhesion.* Nanoscale, 2013. **5**(10): p. 4094-104.
56. Deng, X., et al., *Application of atomic force microscopy in cancer research.* Journal of Nanobiotechnology, 2018. **16**(1): p. 102.
57. Bunaciu, A.A., E. UdriŞTioiu, and H. Aboul-Enein, *X-Ray Diffraction: Instrumentation and Applications.* Critical reviews in analytical chemistry / CRC, 2015. **45**.
58. Foner, H.A. and N. Adan, *The Characterization of Papers by X-Ray Diffraction (XRD): Measurement of Cellulose Crystallinity and Determination of Mineral Composition.* Journal of the Forensic Science Society, 1983. **23**(4): p. 313-321.
59. Weckhuysen, B., *Ultraviolet-Visible Spectroscopy*. 2004.
60. Hussain, A., *UV-VISIBLE SPECTROMETRY*. 2019.
61. Tebyetekerwa, M., et al., *Mechanisms and Applications of Steady-State Photoluminescence Spectroscopy in Two-Dimensional Transition-Metal Dichalcogenides.* ACS Nano, 2020. **14**(11): p. 14579-14604.
62. Gfroerer, T., *Photoluminescence in Analysis of Surfaces and Interfaces*. 2006.
63. Aoki, T., *Characterization of Materials*. 2012.
64. Rostron, P. and D. Gerber, *Raman Spectroscopy, a review.* International Journal of Engineering and Technical Research, 2016. **6**: p. 50-64.
65. Bumbrah, G.S. and R.M. Sharma, *Raman spectroscopy – Basic principle, instrumentation and selected applications for the characterization of drugs of abuse.* Egyptian Journal of Forensic Sciences, 2016. **6**(3): p. 209-215.
66. Chowdhury, S., P. Venkateswaran, and D. Somvanshi. *Optical and Electrical Characterization of n-MoS2/p-Si Heterojunction Diode*. in *2020 IEEE International IOT, Electronics and Mechatronics Conference (IEMTRONICS)*. 2020.
67. Wang, X., et al., *Graphene-like WSe2 nanosheets for efficient and stable hydrogen evolution.* Journal of Alloys and Compounds, 2017. **691**: p. 698-704.
68. Salitra, G., et al., *Highly oriented WSe2 thin films prepared by selenization of evaporated WO3.* Thin Solid Films, 1994. **245**(1): p. 180-185.
69. Zhang, B.-Q., et al., *Synthesis of ultrathin WSe2 nanosheets and their high-performance catalysis for conversion of amines to imines.* Nanoscale, 2018. **10**(43): p. 20266-20271.
70. Beal, A., J. Knights, and W. Liang, *Transmission spectra of some transition metal dichalcogenides. II. Group VIA: Trigonal prismatic coordination.* Journal of Physics C: Solid State Physics, 2001. **5**: p. 3540.
71. Tonndorf, P., et al., *Photoluminescence emission and Raman response of monolayer MoS2, MoSe2, and WSe2.* OPTICS EXPRESS, 2013. **21**: p. 4908-4916.
72. Hang, D.-R., et al., *Facile Bottom-up Preparation of WS2-Based Water-Soluble Quantum Dots as Luminescent Probes for Hydrogen Peroxide and Glucose.* Nanoscale Research Letters, 2019. **14**(1): p. 271.
73. Singh, V.K., et al., *WS2 Quantum Dot Graphene Nanocomposite Film for UV Photodetection.* ACS Applied Nano Materials, 2019. **2**(6): p. 3934-3942.
74. Ren, X., et al., *One-step hydrothermal synthesis of monolayer MoS2 quantum dots for highly efficient electrocatalytic hydrogen evolution.* Journal of Materials Chemistry A, 2015. **3**(20): p. 10693-10697.

75. Rao, C.N.R., H.S.S. Ramakrishna Matte, and U. Maitra, *Graphene Analogues of Inorganic Layered Materials.* Angewandte Chemie International Edition, 2013. **52**(50): p. 13162-13185.
76. Xu, S., D. Li, and P. Wu, *One-Pot, Facile, and Versatile Synthesis of Monolayer MoS2/WS2 Quantum Dots as Bioimaging Probes and Efficient Electrocatalysts for Hydrogen Evolution Reaction.* Advanced Functional Materials, 2015. **25**(7): p. 1127-1136.
77. Bayat, A. and E. Saievar-Iranizad, *Synthesis of blue photoluminescent WS2 quantum dots via ultrasonic cavitation.* Journal of Luminescence, 2017. **185**: p. 236-240.
78. Mattheiss, L.F., *Band Structures of Transition-Metal-Dichalcogenide Layer Compounds.* Physical Review B, 1973. **8**(8): p. 3719-3740.
79. Ben Brahim, N., et al., *Synthesis, characterization and spectral temperature-dependence of thioglycerol-CdSe nanocrystals.* Journal of Luminescence, 2016. **177**: p. 402-408.
80. Laatar, F., et al., *Fabrication of CdSe nanocrystals using porous anodic alumina and their optical properties.* Journal of Luminescence, 2016. **178**: p. 13-21.
81. Yin, W., et al., *Rational Control of Size and Photoluminescence of WS2 Quantum Dots for White Light-Emitting Diodes.* ACS Applied Materials & Interfaces, 2018. **10**(50): p. 43824-43830.
82. Frey, G., et al., *Raman and resonance Raman investigation of MoS_ {2} nanoparticles.* Phys. Rev. B, 1999. **60**.
83. Pallikkarathodi Mani, N. and J. Cyriac, *Hydrothermal synthesis of WS2 quantum dots and their application as a fluorescence sensor for the selective detection of 2,4,6-trinitrophenol.* New Journal of Chemistry, 2020. **44**(26): p. 10840-10848.